

UNIVERSITÀ DEGLI STUDI DI TRIESTE

Sede Amministrativa del Dottorato di Ricerca

Posto di dottorato attivato grazie al contributo della
Sincrotrone Trieste S.C.p.A.

XXIII CICLO DEL DOTTORATO DI RICERCA IN
INGEGNERIA DELL'INFORMAZIONE

Research and Applications of Radio-Frequency Deflecting Cavities

Settore scientifico-disciplinare ING-INF/02 – Campi Elettromagnetici

DIRETTORE DELLA SCUOLA DI
DOTTORATO DI RICERCA
Chiar.mo Prof. Ing. Walter Ukovich
(Università di Trieste)

RELATORE
Chiar.mo Prof. Ing Roberto Vescovo
(Università di Trieste)

DOTTORANDO
Ing. Marco Petronio

TUTORE
Chiar.mo Prof. Ing. Roberto Vescovo
(Università di Trieste)

CORRELATORE
Dr. Ing. Paolo Craievich
(Sincrotrone Trieste S.C.p.A.)

ANNO ACCADEMICO 2009/2010

*Ad Antonella,
a Mamma e
a Papà*

Contents

Introduction	4
1 RF Deflectors	6
1.1 FERMI@Elettra Layout	6
1.2 Deflecting cavities	10
1.3 Energy exchange in the deflector	11
1.4 Beam optics	15
1.5 Transport matrix	19
1.6 Bunch length measurement	20
2 Low Energy Deflector	25
2.1 Installation layout	25
2.2 RF design	28
2.3 Bead-pull measurements	32
2.4 Bunch compressor	35
2.5 Optical layout	36
3 Bunch Measurements	39
3.1 Calibration	39
3.2 Bunch length measurement	44
3.3 Profile reconstruction	46
3.4 Instrument resolution	50
3.5 Quadrupole scan	52
3.6 Emittance measurement	54
3.7 Emittance slice measurement	56

<i>CONTENTS</i>	3
4 High Energy Deflectors	60
4.1 Technical specifications	60
4.2 Group velocity derivation	61
4.3 Shunt resistance and deflecting voltage	63
4.4 Basic cell design	68
4.5 A detuning error theory	72
4.6 Coupler design	77
5 Transversal Wakefield	83
5.1 Wakefield effect	83
5.2 Transversal beam dynamics	85
5.3 Determining the bunch motion	86
5.4 Numerical examples	89
5.5 Evaluating the convergence	98
Conclusion	99

Introduction

The radio-frequency deflectors are travelling wave disk loaded structures in which an electromagnetic field can interact with ultra-relativistic electron bunches, providing a constant transversal force. These devices have been used in the accelerator physics from the early 60', when they were employed as separators of particles having different charges. During the last years, with the development of the fourth generation light sources, they have been re-discovered as a beam diagnostic tool, and used to analyze important properties such the bunch length and the slice emittance.

Radio-frequency deflectors have been involved in the FERMI@Elettra project, which is a fourth generation light source under development at the Elettra Laboratory of Trieste, Italy. In particular, two travelling wave deflectors will be placed just before the undulators chains, where the free electron laser occurs, while another standing wave deflector has been installed in the first part of the machine, after the first bunch compressor.

This thesis has the aim of describing these instruments. Precisely, such devices have designed with the electromagnetic code HFSS, and their interaction with the electron beam has been analyzed with new numerical techniques.

In the first chapter of this thesis a brief overview of the FERMI@Elettra project is given, introducing the basic deflecting theory and some related aspects of the accelerator physics. In the second chapter the radio-frequency design of the low energy deflector is presented; the design has been carried out in collaboration with the SPARC Laboratory of Frascati and University La Sapienza (Roma). The second chapter provides a detailed description of the low energy deflector installation setup and of the devices involved in the bunch measurements.

The third chapter reports measurement results on the electron bunch, which is the main application of the radio-frequency deflector as a beam diagnostic tool. Both bunch length measurements and slice emittance measurements are discussed, with the reconstruction of the bunch longitudinal profile, the estimation of the peak current and an indirect measurement of the bunch compressor area optics.

In the fourth chapter the theory and the radio-frequency design of the high energy deflectors are summarized: the first measurements performed on the copper basic cell confirm the value predicted by the electromagnetic code. Furthermore, the chapter includes a new simple theory, which allows the explanation of the energy exchange degradation between the electromagnetic field and the particles. In particular, the method can be used to take into account the mechanical errors in the basic cell realization.

In the last chapter, a new algorithm is presented, that allows to determine the transversal bunch motion in presence of wakefields in a radio-frequency deflector. The algorithm is employed to evaluate the wakefield effects in the high energy deflectors, and can be used for any charge distribution and for any initial condition of the bunch at the input section of the cavity. In particular, the errors produced by the transversal wakefields in a bunch length measurement are analyzed with significant examples.

As a conclusion, in this thesis both research and applications of radio-frequency deflectors are treated. With reference to the applications, the standing wave deflector has been used to analyze the properties of the FERMI@Elettra electron bunches. Such bunches have produced the first free electron laser radiation in December 2010. From the research viewpoint, the thesis proposes an advance in the wakefield analysis, which has permitted the simulations of the wakefields instability effects on the bunch travelling in the high energy deflectors.

Chapter 1

RF Deflectors

1.1 FERMI@Elettra Layout

The FERMI@Elettra project is a fourth generation light source under development at Elettra laboratory of the Trieste [1], based on the Free-Electron-Laser (FEL) technology. It will be a national and international user facility for scientific investigations with high brilliance X-ray pulses of ultra-fast and ultra-high resolution processes in material science and physical biosciences. The FERMI@Elettra project will consist of a linear accelerator plus two FEL beam lines, FEL1 and FEL2. A schematic layout is shown in Fig. 1.1.

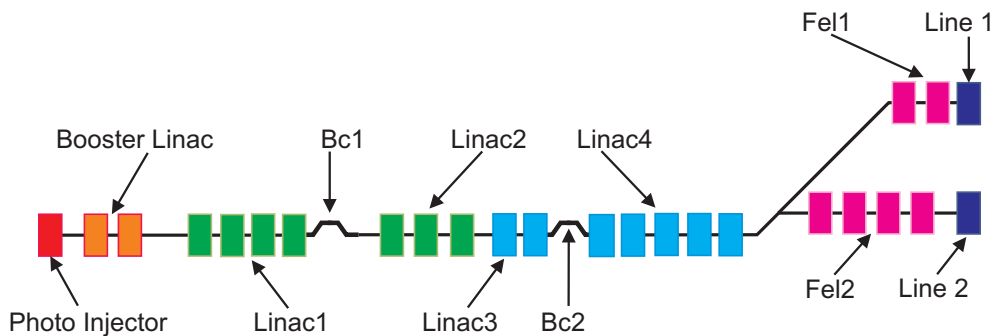


Figure 1.1: *Schematic layout of the FERMI@Elettra Project.*

The first part of the machine is the photo-injector (Fig. 1.2), based on an electron gun which produces electron bunches temporized from 10 Hz to

50 Hz. The charge extracted will be 0.8-1 nC in the standard operations of the machine. After the photo-injector, the beam is accelerated by five accelerating sections. The first one, called booster linac, increases the beam energy up to 100 MeV.

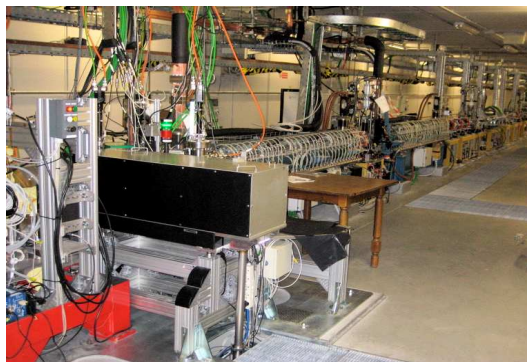


Figure 1.2: *The photo-injector and the booster linac.*

After the booster linac, another accelerating section, named linac 1, accelerates the bunch up to 350 MeV (Fig. 1.3).



Figure 1.3: *The linac 1 accelerating section.*

A first bunch compressor Bc1, which is based on a magnetic chicane, is

then used to compress the electron bunch up to a factor ten, thus increasing the peak current and changing the longitudinal bunch shape (Fig. 1.4).

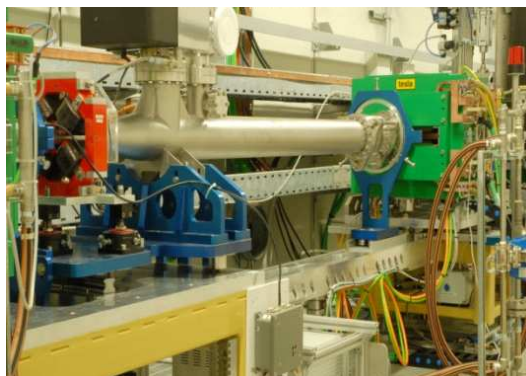


Figure 1.4: *The bunch compressor Bc1.*

The successive three accelerating sections, named linac 2, linac 3 and linac 4, raise the beam energy to 1.2 GeV (Fig. 1.5). A second bunch compressor (Bc2) will be placed between linac3 and linac4.



Figure 1.5: *The accelerating sections from linac 2 to linac 4.*

The last part of the machine will be composed by two lines, where the free electron laser process will occur. Each line will be composed by an undulator

chain installation (Fig. 1.6), followed by a photon transport line and by an experimental hall where the radiation will be analyzed.



Figure 1.6: *An undulator used in the FERMI@Elettra Project.*

In the FERMI@Elettra Project the free-electron-laser will operate in the 100-20 nm energy region in FEL1 and down to 4 nm in FEL2. Both FEL lines are based on the principle of high gain, harmonic generation free electron laser amplifier employing multiple undulators, up-shifting an initial seed laser having a 240-300 nm wavelength. In the first part the electron beam will interact with a first undulator called "modulator", which will induce a energy modulation. Then the magnetic field of a dispersive section will convert the energy modulation into spatial modulation at the harmonics of the wavelength of the seed laser. Thus the bunched electrons emit coherent radiation in a second undulator (the "radiator") tuned at a higher harmonic corresponding to the desired FEL output. The FEL2 configuration foresees another stage of modulator-dispersive section-radiator in order to reach the design wavelength of 4 nm.

It is important to remark that the FERMI@Elettra Project was under construction during the period of this thesis. In particular, the installations of the photo-injector, booster linac, the first bunch compressor and of the accelerating section from linac 1 to linac 4, have been already completed in the last months of 2010 and also the first FEL line started the first operations with the beam.

1.2 Deflecting cavities

An RF deflector is a travelling wave disk loaded structure, composed by the repetition of a basic cell, as is shown in Fig. 1.7.

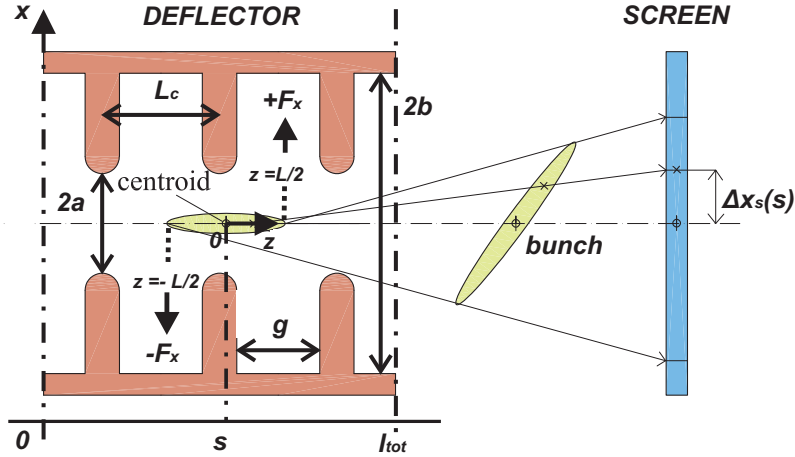


Figure 1.7: An electron bunch stretched in a radio frequency deflector. The local abscissa z is referred to the bunch center and the global abscissa s is referred to the input section of the deflector.

The geometrical parameters of the basic cell are the iris radius a , the cell length L_c , the external radius b and the internal cell gap g ; the total length of the structure is l_{tot} .

The geometric structure of the deflector is designed to allow the propagation of hybrid modes, which have both a longitudinal electric field component and a longitudinal magnetic field component. The reason is that neither a TE mode nor a TM mode can impart a transversal momentum to a bunch travelling approximately at the speed of the light in the vacuum [2]. The hybrid deflecting mode is called HEM_{11} , which has a phase velocity synchronous with the speed of the relativistic electron bunch and allows an effective energy exchange, as described by the Panofsky-Wenzel theorem [3]. Radio-frequency deflectors are used to perform bunch length measurements and phase space diagnostics in the light source accelerators [4], [5]. When the deflector is turned on, the electron bunch is stretched on axis by a transversal deflecting voltage and is forced to collide with a detector screen, as illustrated

in Fig. 1.7. The beam trace on the screen is then converted into an optical signal to be processed. When the deflector is turned off, the detector screen is removed and the beam simply passes through the device without being deflected, and is used to produce a free electron laser (FEL) radiation.

The low energy RF deflector of the FERMI@Elettra has been already installed after the first bunch compressor at the end of 2009, and has done the first operation with the electron beam during the last months of 2010. It is a half-meter long standing wave cavity composed by five cells operating at low energy, $E_{tot}=350$ MeV. The two high energy deflectors, which are still under construction, will be installed after the second bunch compressor, just before that the FEL process starts. They are travelling wave structures two meters and half long, composed by seventy-two cells plus two couplers, operating at high energy, $E_{tot}=1.2$ GeV.

1.3 Energy exchange in the deflector

Since the RF deflector has a spatial period L_c in the s direction, the Floquet theorem can be applied. Such theorem states that, in a periodic structure of period L_c , the electromagnetic field between two sections separated by a period are equals except than a complex factor, thus:

$$E = e(T, s)e^{-\gamma_0 s} \quad (1.1)$$

where E is the electric field, $e(T, s)$ is periodic in s of period L_c and T represents the transversal coordinates, and γ is the propagation constant [6], [7]. Considering a free-loss medium $\gamma_0 = j\beta_0$ in equation (1.1), the electromagnetic field has the phase advance

$$\phi = \beta_0 L_c \quad (1.2)$$

where β_0 is the phase constant. Since $e(T, s)$ is periodic in s of period L_c , expanding in a Fourier series we obtain:

$$\begin{cases} e(T, s) = \sum_{-\infty}^{+\infty} e_n(T) e^{-j \frac{2\pi n}{L_c} s} \\ e_n = \frac{1}{L_c} \int_0^{L_c} e(T, s) e^{j \frac{2\pi n}{L_c} s} ds \end{cases} \quad (1.3)$$

and the field can be written as:

$$E = \sum_{-\infty}^{+\infty} \left[e_n(T) e^{-j \frac{2\pi n}{L_c} s} \right] e^{-j \beta_0 s} = \sum_{-\infty}^{+\infty} e_n(T) e^{-j \beta_n s} \quad (1.4)$$

where:

$$\beta_n = \beta_0 + \frac{2\pi}{L_c} n \quad (1.5)$$

is the phase constant of the n -th spatial harmonic. From equation (1.5) we can see that in a periodic structure the electromagnetic field is the sum of infinite spatial harmonics of different phase velocity $v_{p,n}$:

$$v_{p,n} = \frac{\omega}{\beta_n} = \frac{\omega}{\beta_0 + \frac{2\pi}{L_c} n}. \quad (1.6)$$

The electromagnetic field is characterized by a single group velocity, since for every spatial harmonic we can write:

$$v_{g,n} = \frac{d\omega}{d\beta_n} = \left(\frac{d\beta}{d\omega} \right)^{-1} = \left(\frac{d\beta_0}{d\omega} \right)^{-1} \quad (1.7)$$

thus the spatial harmonics have the same group velocity:

$$v_g = \left(\frac{d\beta_0}{d\omega} \right)^{-1} \quad (1.8)$$

The transversal energy exchange between the bunch and the electromagnetic field in the radio-frequency deflector is ruled by the Lorentz force:

$$\vec{F}_t = q \left(\vec{E} + \vec{v} \times \vec{B} \right)_t \quad (1.9)$$

where (\vec{E}, \vec{H}) is the electromagnetic field and the subscript "t" means transversal. Thus the total transversal momentum can be written as:

$$\vec{p}_t = \int_0^{l_{tot}} \vec{F}_t dt = \frac{q}{c} \int_0^{l_{tot}} [\vec{E}_t + (\vec{v} \times \vec{B})_t] ds \quad (1.10)$$

where we have supposed that the particles have the speed of light in vacuum c and travel on axis in the s direction. Due to the Panowsky-Wenzell theorem, equation (1.10) can be written as [3], [8], [9]:

$$\vec{p}_t = j \frac{q}{\omega} \int_0^{l_{tot}} \nabla_t E_z e^{j\omega t} ds \quad (1.11)$$

where:

$$\vec{F}_t = \frac{q}{\beta} \nabla_t E_z \quad (1.12)$$

is the expression of the transversal Lorentz force inside the cavity, where the temporal factor $e^{j\omega t}$ is omitted and β is the field phase constant. All the spatial harmonics will interact with the electron bunch according to the Lorentz force of equation (1.9) which leads to expression (1.11), but only the spatial harmonic synchronous with the speed of the beam can produce a net deflection along the device. For a disk-loaded structure, the fundamental harmonic of the deflecting mode has been calculated analytically for an electromagnetic field travelling at the speed of the light [2]. The HEM_{11} mode has the expression [4]:

$$\begin{cases} E_r = j \frac{E_0}{4} [k^2 a^2 + k^2 r^2] \cos \vartheta \\ E_\vartheta = -j \frac{E_0}{4} [k^2 a^2 - k^2 r^2] \sin \vartheta \\ E_z = E_0 k r \cos \vartheta \end{cases} \quad (1.13)$$

and:

$$\begin{cases} Z_0 H_r = -j \frac{E_0}{4} [k^2 a^2 - 4 - k^2 r^2] \sin \vartheta \\ Z_0 H_\vartheta = j \frac{E_0}{4} [k^2 a^2 - 4 + k^2 r^2] \cos \vartheta \\ Z_0 H_z = E_0 k r \sin \vartheta \end{cases} \quad (1.14)$$

where E_0 is a constant, Z_0 is the vacuum impedance, k is the free space wave number, r and θ are the radial and the azimuthal coordinate, respectively; the propagation factor $e^{-j\beta s}$ has been omitted. Since $x = r \cos \theta$, in equation (1.13) we can write $E_z = E_0 k x$, thus using (1.12) we obtain:

$$\begin{cases} F_x = q E_0 \\ F_y = 0 \end{cases} \quad (1.15)$$

because $\beta = k$ at the speed of the light. Equation (1.15) describes the transversal force inside the deflector, which is constant inside the iris of the structure, and for this reason the HEM_{11} is referred as an aberration free mode.

The contribute of every spatial harmonic in the beam deflection can be considered evaluating the longitudinal electric field, which for equation (1.4) has the expression:

$$E_z = \sum_{n=0}^{\infty} e_{z,n}(T) e^{j(\omega t - \beta_n s)} \quad (1.16)$$

where we have multiplied the field by the temporal factor $e^{j\omega t}$. The integral (1.16), which describes the energy exchange inside the deflector, can be particularized by means of equation (1.11) in:

$$\vec{p}_t = q \sum_{n=0}^{\infty} \left(\int_0^{l_{tot}} \frac{\nabla_t e_{z,n}(T)}{\beta_n} e^{-j\beta_n s} e^{j\beta_0 s} ds \right) \quad (1.17)$$

which using (1.5) becomes:

$$\vec{p}_t = q \sum_{n=0}^{\infty} \frac{\nabla_t e_{z,n}(T)}{\beta_n} \left(\int_0^{l_{tot}} e^{-j\frac{2\pi}{L_c} ns} ds \right) \quad (1.18)$$

Since the RF deflector length is given by $l_{tot} = nL_c$, where n is the cell number, $\int_0^{l_{tot}} e^{-j\frac{2\pi}{L_c} ns} ds$ is different from zero only if $n = 0$, thus we have proved that only the fundamental harmonic fully interact with the beam. The other spatial harmonics can deliver a local force, but the total effect is negligible because they are not synchronous with the bunch.

In the RF design the synchronism condition of the fundamental harmonic with the bunch, is imposed choosing properly the cell length L_c . In fact, once the periodic phase advance ϕ has been fixed, L_c can be calculated by equation (1.2), where $\beta_0 = \frac{\omega}{v_{p,0}}$ by equation (1.6). Assuming a beam velocity equal to the speed of light and a fundamental spatial harmonic synchronous with the beam, we have $v_p = c$ and $\frac{\omega}{c} = \beta_0$. Thus the cell length L_c which allows a correct interaction between the fundamental harmonic and the electron bunch is simply given by

$$L_c = c \frac{\phi}{\omega} \quad (1.19)$$

1.4 Beam optics

In a linear accelerator the beam is guided along a design orbit by using magnetic lenses, such as magnetic quadrupoles, dipoles and correctors. In particular, quadrupoles magnets are used for focusing and defocusing the beam, and in the ideal case they produce a constant transverse quadrupole gradient [9]:

$$G = \frac{\partial B_x}{\partial y} = \frac{\partial B_y}{\partial x} \quad (1.20)$$

From the Lorentz force we obtain:

$$\begin{cases} F_x = -evGx \\ F_y = evGy \end{cases} \quad (1.21)$$

where v is the speed of the particle which is travelling in the z direction. We can note that if $eG > 0$ the quadrupole is focusing in x and defocusing in y , while if $eG < 0$ the device works in the opposite condition. From equation (1.21) we can derive the motion equation:

$$\begin{cases} \frac{d^2x}{ds^2} + \bar{\kappa}^2(s)x = 0 \\ \frac{d^2y}{ds^2} - \bar{\kappa}^2(s)y = 0 \end{cases} \quad (1.22)$$

where $\bar{\kappa}^2(s) = \frac{eG(s)}{m\gamma v}$. Both equations (1.22) are in the form:

$$\ddot{x} + \bar{K}(s)x = 0 \quad (1.23)$$

which is called Hill's equation. It can be shown that the generic solution of equation (1.23) can be written as [10]:

$$x(s) = \sqrt{\varepsilon_x \bar{\beta}_x(s)} \cos(\bar{\phi}_x(s) + \bar{\phi}_{x,1}) \quad (1.24)$$

where $\bar{\beta}_x(s)$ and $\bar{\phi}_x(s)$ are called the betatron function and the phase function, respectively, while ε_x and $\bar{\phi}_{x,1}$ are two constants. The constant ε_x is called emittance. The functions $\bar{\beta}_x(s)$ and $\bar{\phi}_x(s)$ are related as follow:

$$\bar{\phi}_x = \int_{s_0}^s \frac{1}{\bar{\beta}_x(u)} du \quad (1.25)$$

Using the betatron function we can define the functions:

$$\bar{\alpha}_x(s) = -\frac{1}{2} \frac{d\bar{\beta}_x(s)}{ds} \quad (1.26)$$

and

$$\bar{\gamma}_x(s) = \frac{1 + \bar{\alpha}_x(s)}{\bar{\beta}_x(s)} \quad (1.27)$$

$\bar{\beta}_x(s)$, $\bar{\alpha}_x(s)$ and $\bar{\gamma}_x(s)$ are called Twiss parameters and provide a complete description of the beam motion, which is used in the accelerator physics. In particular, the transversal position x and the transversal derivative x' , which is called angular divergence, are related by the Twiss parameters by means of the relation [10]:

$$\bar{\gamma}_x(s) x^2 + 2\bar{\alpha}_x(s) x + \bar{\beta}_x(s) x'^2 = \epsilon_x \quad (1.28)$$

which is the equation of an ellipse centered in $(\bar{x}, \bar{x}') = (0, 0)$ and area $\pi\epsilon_x$ in the phase space of the coordinates (x, x') . It can be shown [11] that the motion of a single particle from an initial point s_0 to a final point s in the phase space can be given by the transport matrix R_x :

$$\begin{pmatrix} x(s) \\ x'(s) \end{pmatrix} = \begin{pmatrix} R_{11} & R_{12} \\ R_{21} & R_{22} \end{pmatrix} \begin{pmatrix} x(s_0) \\ x'(s_0) \end{pmatrix} \quad (1.29)$$

and the total transport matrix of two or more consecutive elements is given by the product of the respective transport matrices. The matrix R_x can be particularized in terms of Twiss functions as:

$$\begin{pmatrix} \sqrt{\frac{\bar{\beta}_{x,s}}{\bar{\beta}_{x,s_0}}} (\cos \bar{\phi}_{x,s-s_0} + \bar{\alpha}_{x,s_0} \sin \bar{\phi}_{x,s-s_0}) & \sqrt{\bar{\beta}_{x,s} \bar{\beta}_{x,s_0}} \sin \bar{\phi}_{x,s-s_0} \\ -\frac{1 + \bar{\alpha}_{x,s} \bar{\alpha}_{x,s_0}}{\sqrt{\bar{\beta}_{x,s} \bar{\beta}_{x,s_0}}} \sin \bar{\phi}_{x,s-s_0} & \sqrt{\frac{\bar{\beta}_{x,s}}{\bar{\beta}_{x,s_0}}} (\cos \bar{\phi}_{x,s-s_0} - \bar{\alpha}_{x,s} \sin \bar{\phi}_{x,s-s_0}) \end{pmatrix} \quad (1.30)$$

where $\bar{\beta}_{s,x}$, $\bar{\alpha}_{s,x}$ and $\bar{\beta}_{x,s_0}$, $\bar{\alpha}_{x,s_0}$ are the Twiss functions evaluated at the longitudinal coordinates s and s_0 , respectively; $\bar{\phi}_{x,s-s_0}$ represents the optical phase advance between s and s_0 . In the vertical plane the transport matrix R_y has the expression:

$$\begin{pmatrix} y(s) \\ y'(s) \end{pmatrix} = \begin{pmatrix} R_{33} & R_{34} \\ R_{43} & R_{44} \end{pmatrix} \begin{pmatrix} y(s_0) \\ y'(s_0) \end{pmatrix} \quad (1.31)$$

and matrix R_y can be particularized as:

$$\begin{pmatrix} \sqrt{\frac{\bar{\beta}_{y,s}}{\bar{\beta}_{y,s_0}}} (\cos \bar{\phi}_{y,s-s_0} + \bar{\alpha}_{y,s_0} \sin \bar{\phi}_{y,s-s_0}) & \sqrt{\bar{\beta}_{y,s} \bar{\beta}_{y,s_0}} \sin \bar{\phi}_{y,s-s_0} \\ -\frac{1+\bar{\alpha}_{y,s} \bar{\alpha}_{y,s_0}}{\sqrt{\bar{\beta}_{y,s} \bar{\beta}_{y,s_0}}} \sin \bar{\phi}_{y,s-s_0} & \sqrt{\frac{\bar{\beta}_{y,s}}{\bar{\beta}_{y,s_0}}} (\cos \bar{\phi}_{y,s-s_0} - \bar{\alpha}_{y,s} \sin \bar{\phi}_{y,s-s_0}) \end{pmatrix} \quad (1.32)$$

The motion of an electron distribution $\rho(x)$ can be described by means of the beam matrix [11]

$$\bar{\sigma}_x = \begin{bmatrix} \langle x^2 \rangle & \langle x x' \rangle \\ \langle x x' \rangle & \langle x'^2 \rangle \end{bmatrix} \quad (1.33)$$

where we have indicated with

$$\langle x \rangle = \frac{\int_{-\infty}^{+\infty} x \rho(x) dx}{\int_{-\infty}^{+\infty} \rho(x) dx} \quad (1.34)$$

the first moment of the beam distribution, and with

$$\langle x^2 \rangle = \frac{\int_{-\infty}^{+\infty} x^2 f(x) dx}{\int_{-\infty}^{+\infty} f(x) dx} \quad (1.35)$$

the second moment of the beam distribution. The Twiss parameters $(\bar{\beta}_{e,x}, \bar{\alpha}_{e,x}, \bar{\gamma}_{e,x})$ of an electron distribution can be defined from the beam matrix of equation (1.33) as:

$$\frac{\bar{\sigma}_x}{\det(\bar{\sigma}_x)} = \begin{bmatrix} \bar{\beta}_{e,x} & -\bar{\alpha}_{e,x} \\ -\bar{\alpha}_{e,x} & \bar{\gamma}_{e,x} \end{bmatrix} \quad (1.36)$$

where the quantity:

$$\varepsilon_x = \sqrt{\det(\bar{\sigma}_x)} \quad (1.37)$$

is called RMS emittance and the product $\pi\varepsilon_x$ is the ellipse area in the phase space. From equation (1.37) we have

$$\varepsilon_x = \sqrt{\langle x^2 \rangle \langle x'^2 \rangle - \langle x x' \rangle^2} \quad (1.38)$$

The motion of the electron beam distribution from an initial point s_0 to a final point s can be described in terms of the beam matrix as

$$\bar{\sigma}_x(s_2) = R_x \sigma_x(s_1) R_x^T \quad (1.39)$$

where R_x is the transport matrix of equation (1.30) written in terms of the Twiss parameters of the electron distribution.

1.5 Transport matrix

The transport matrix in equation (1.30) can be particularized for each optical element which compose a linear accelerator. This can be done by solving the Hill differential equation (1.22) and determining the relationship between the phase space coordinates (x, x') from the input section to the output section of the optical element. As an example, for a drift space of length l we have simply $\bar{\kappa} = 0$ in equation (1.22), and the transport matrix is simply given by:

$$R_x = R_y = \begin{pmatrix} 1 & l \\ 0 & 1 \end{pmatrix} \quad (1.40)$$

For a quadrupole magnet, considering $\bar{\kappa} > 0$ in equation (1.22) we obtain

$$R_x = \begin{pmatrix} \cosh \bar{v} & \frac{1}{\sqrt{|\bar{\kappa}|}} \sinh \bar{v} \\ \sqrt{|\bar{\kappa}|} \sinh \bar{v} & \cosh \bar{v} \end{pmatrix} \quad (1.41)$$

and

$$R_y = \begin{pmatrix} \cosh \bar{v} & \frac{1}{\sqrt{|\bar{\kappa}|}} \sinh \bar{v} \\ -\sqrt{|\bar{\kappa}|} \sinh \bar{v} & \cosh \bar{v} \end{pmatrix} \quad (1.42)$$

where $\bar{v} = \sqrt{|\bar{\kappa}| \bar{l}}$ and \bar{l} is the device length. We can observe that R_x and R_y represent the horizontal defocusing and the vertical focusing, respectively. If $\bar{\kappa} < 0$, R_x and R_y are interchanged, thus we obtain horizontal focusing and vertical defocusing, respectively. If the focal length \bar{f} of the quadrupole is much larger than the length of the quadrupole, the following "thin-lens" condition holds [11]:

$$\bar{f} = \frac{1}{\bar{\kappa} \bar{l}} \gg \bar{l} \quad (1.43)$$

and the transfer matrices (1.41) and (1.42) simplify in:

$$R_x = \begin{pmatrix} 1 & 0 \\ 1/\bar{f} & 1 \end{pmatrix} \quad (1.44)$$

$$R_y = \begin{pmatrix} 1 & 0 \\ -1/\bar{f} & 1 \end{pmatrix} \quad (1.45)$$

We will refer to the quantity $\bar{Z} = 1/\bar{f}$ as the integrated field strength of the quadrupole.

1.6 Bunch length measurement

The transversal beam motion of a deflecting cavity operating in the x direction is given by:

$$F_x = \frac{dp_x}{dt} \quad (1.46)$$

where p_x is the horizontal momentum. From equation (1.46) we obtain:

$$p_x = \int_0^{l_{tot}} F_x dt \quad (1.47)$$

Since $p_x = \gamma m \frac{dx}{dt}$ and $s = ct$ at the speed of the light, equation (1.47) reduces to:

$$\frac{dx}{ds} = \frac{F_x l_{tot}}{E_{tot}} \quad (1.48)$$

which represents the variation of the transversal coordinate x with respect to the longitudinal coordinate s . We will refer to $\Delta\dot{x} = \frac{dx}{ds}$ as the angular divergence, or the transversal kick. The transversal deflecting voltage can be defined as:

$$V_t = \frac{l_{tot} F_x}{q} \quad (1.49)$$

The electromagnetic field is applied to the bunch at $f = 2.998$ GHz, and a factor $\sin(kz + \phi_{RF})$ must be included in our considerations, where ϕ_{RF} is the phase delay of the bunch center with respect to the wavefront of the field. With this positions equation (1.48) becomes:

$$\Delta\dot{x} = q \frac{V_t}{E_{tot}} \sin(kz + \phi_{RF}) \quad (1.50)$$

which represents the transversal kick received by the electron bunch. For a RF deflector operating at $f=2.998$ GHz, we have $k = 62.8$ rad/m, thus for a standard beam some millimeters long we can assume $|kz| \ll 1$. Therefore equation (1.50) reduces to:

$$\Delta\dot{x} = q \frac{V_t}{E_{tot}} (kz \cos \phi_{RF} + \sin \phi_{RF}) \quad (1.51)$$

Let us note that if $\phi_{RF} = 0$, which is called the zero-crossing condition, equation (1.51) reduces to:

$$\Delta\dot{x} = q \frac{V_t}{E_{tot}} kz \quad (1.52)$$

which describes the linear correlation between the angular divergence at the output section of the deflector and the bunch longitudinal coordinate z . Equation (1.52) is used to perform the beam diagnostics with the radio-frequency deflector, in particular to investigate the longitudinal beam properties by means of the observation of a deflected trace on a screen, as will be shown in chapter 2.

From equation (1.29) we can see that the position of a particle on the screen is related to the angular divergence by:

$$\Delta x_S = R_{12} \Delta\dot{x} \quad (1.53)$$

where $R_{12} = \sqrt{\bar{\beta}_S \bar{\beta}_D} \sin \bar{\phi}_{DS}$ by equation (1.30), $\bar{\beta}_S$ and $\bar{\beta}_D$ are the value of the betatron function evaluated at the screen and at the deflector, respectively, and $\bar{\phi}_{DS}$ is the optical phase advance. The excursion of the particle at the screen location can be obtained using equations (1.51) and (1.53):

$$\Delta x_S = q \frac{V_t}{E_{tot}} (kz \cos \phi_{RF} + \sin \phi_{RF}) R_{12} \quad (1.54)$$

The transverse centroid offset at the screen can be evaluated by averaging equation (1.54) over z . Under the assumption of $\langle z \rangle = 0$, we have:

$$\bar{\Delta} x_S = \frac{eV_t}{E} R_{12} \sin \phi_{RF} \quad (1.55)$$

while the beam size standard deviation at the screen is given by:

$$\sigma_{x,S} = q \frac{V_t}{E_{tot}} \sigma_z k R_{12} \cos \phi_{RF} \quad (1.56)$$

Thus, at the zero-crossing condition, we obtain from equations (1.55) and (1.56):

$$\begin{cases} \bar{\Delta}x_S = 0 \\ \sigma_{x,S} = q \frac{V_t}{E_{tot}} \sigma_z R_{12} \end{cases} \quad (1.57)$$

Hence we can observe that, if $\phi_{RF} = 0$, the centroid of the bunch remains on axis, while $\sigma_{x,S}$ reaches its maximum value. In this way the bunch is stretched on axis and the trace on the screen has the maximum deflection. We can observe that equation (1.54) at zero crossing simplifies as follows:

$$\Delta x_S = q \frac{V_t R_{12}}{E_{tot}} k z \quad (1.58)$$

from which we obtain

$$z = q \frac{V_t R_{12}}{E_{tot}} k \Delta x_S \quad (1.59)$$

which can be used to re-construct the longitudinal profile of the bunch.

Since in the real case the electron bunch has a transverse finite dimension $\sigma_{x,0}$, a trace at the screen will be observable also when $V_t = 0$. Hence the total standard deviation observed at the screen will be:

$$\sigma_{x,S,R} = \sqrt{\sigma_{x,0}^2 + \sigma_{x,S}^2} \quad (1.60)$$

which by equation (1.56) becomes:

$$\sigma_{x,S,R}^2 = \sigma_{x,0}^2 + \left[q \frac{V_t}{E_{tot}} \sigma_z k R_{12} \right]^2 \quad (1.61)$$

Equation (1.61) can be used to calculate the standard deviation of the bunch length σ_z eliminating the error due to the finite transverse dimension $\sigma_{x,0}$. In fact, using two or more deflecting voltages and evaluating the corresponding $\sigma_{x,S,R}$ calculated at the screen, a parabolic fit $\sigma_{x,S,R}^2 = a + bV_t^2$ can be performed. By means of the quadratic coefficient b , the standard deviation of the bunch length can be estimated as:

$$\sigma_z = \sqrt{b} \frac{E_{tot}}{qkR_{12}} \quad (1.62)$$

Let us note that the error in the determination of $\sigma_{x,S,R}$ is directly proportional to the error on σ_z . Furthermore, the error on the fitting coefficient b decreases when the maximum value of V_t and the number of different deflecting voltage increases.

Chapter 2

Low Energy Deflector

2.1 Installation layout

The low energy radio-frequency deflector (LERFD) is a five cell standing wave structure working in the π -mode, which has been installed in the FERMI@Elettra linac after the BC1 bunch compressor (Fig. 2.1). The cavity has been built in the period 2008/2009 in collaboration with the SPARC Laboratory at INFN-LNF-Frascati, Italy, and with the University of Rome [12], [13]. The radio-frequency design of the cavity has been performed with the electromagnetic code HFSS [14].

The radio-frequency conditioning of the deflector started in June 2010, while the first beam measurements have been done in September 2010. The device shares the same klystron (K1) with the electron gun, thus an attenuator and a phase shifter, placed in the deflector arm, are required to independently modulate the input power, as is shown in Fig. 2.2. The radio-frequency scheme foresees the insertion of a circulator, in order to completely decouple the deflector arm from the gun arm. However, the device was not present during the operations performed in the last months of 2010.

The radio-frequency power travels from the klystron K1 to a sixty meters rectangular waveguide, which is connected to the cavity with a taper. Six vacuum pumps in the rectangular waveguide monitor the vacuum level, while another vacuum pump (P_7) has been placed near the cavity in the linear accelerator. The vacuum level reached the value of $1 \cdot 10^{-9}$ mbar two weeks



Figure 2.1: *The low energy radio-frequency deflector in the FERMI@Elettra linac.*

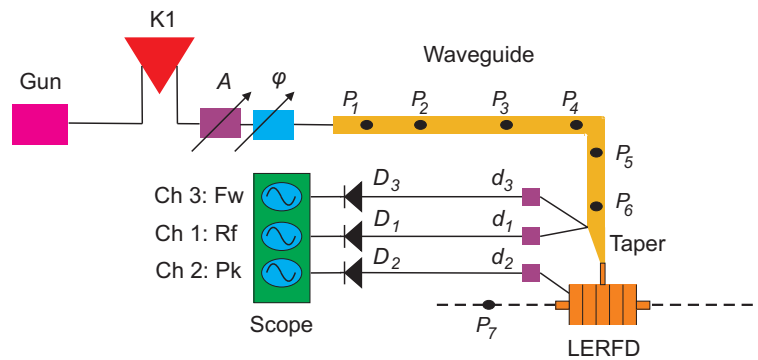


Figure 2.2: *Schematic layout of the low energy deflector: A is the attenuator, φ is the phase shifter, P_i is a vacuum pump ($i = 1..7$), the symbols d_k and D_k are directional couplers and diodes, respectively ($k=1..3$).*

after the cavity installation without input power. In the normal operations, with the RF power traveling in rectangular pulses having a duration of $1.1 \mu\text{s}$ (until October 2010) or $1.2 \mu\text{s}$ (from November 2010) and a repetition rate of 10 Hz, the vacuum level was about $5 \cdot 10^{-8}$ mbar.

A RF setup which allows the estimation of the input power and of the behavior of the cavity, using diodes and directional couplers, has been im-

plemented. In particular, three directional couplers collect a signal that is proportional to the input power, to the reflected power and to the internal field, respectively. The signal proportional to the internal field is picked up from an antenna placed inside the cavity. Since the diodes have been characterized by means of an oscilloscope and a signal generator, and the attenuation of the directional couplers is known, the input power feeding the deflector can be obtained reading the traces at the oscilloscope. Fig. 2.3 (a) shows the input power estimated by the diodes as a function of the attenuation level, during the cavity operations. As it will be shown in section 2.2, the integrated deflecting voltage V_t is related to the input power P_{in} by the relation $V_t = \sqrt{2P_{RF} r_t}$ where r_t is the shunt resistance. Thus also V_t can be calculated and has been reported in Fig. 2.3 (b).

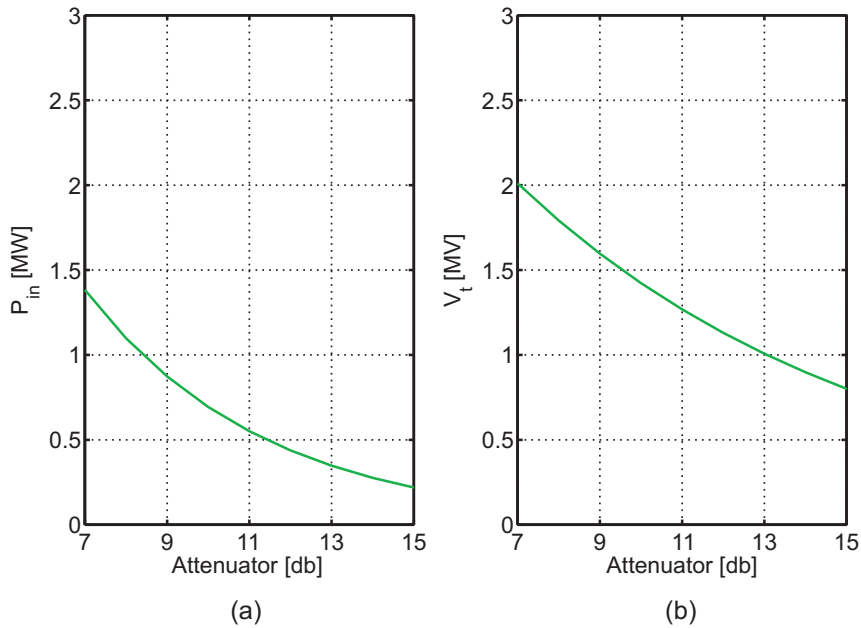


Figure 2.3: (a) Input power estimated by the diode as a function of the attenuation; (b) Deflecting voltage as a function of the attenuation.

2.2 RF design

The main constraints of the RF deflector working in the π -mode and operating in the vertical plane are as follow: integrated deflecting voltage $V_t \geq 3$ MV, working frequency $f=2.99801$ GHz, available input power $P_{in}=5$ MW and filling time $t_F \leq 3\mu s$. The basic cell is shown in Fig. 2.4: the main geometrical parameters are the cell length L_c , the iris radius a , the external radius b and the disk width t .

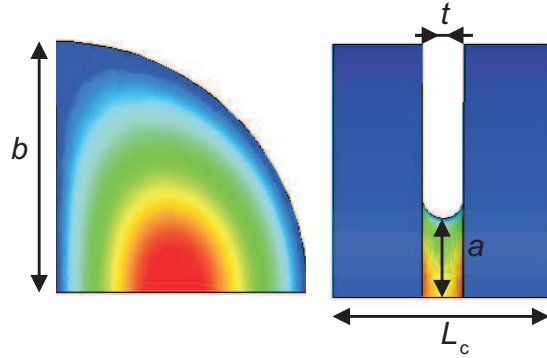


Figure 2.4: *Electric field amplitude in the low energy deflector basic cell.*

The cell length has been calculated using equation (1.19), which gives $L_c=50$ mm. With $a=18$ mm, $t=9.5$ mm $b=57.64$ mm the deflecting π -mode has been excited in the basic cell at the proper working frequency. The sensitivities of the geometrical parameters are reported in Table 2.1: as it was expected, the external radius b and the iris radius a are the most critical parameters for what concerns the mechanical tolerances.

Table 2.1: *Basic Cell Sensitivities.*

a	-20.18 MHz/mm
b	-47.3 MHz/mm
L	2.1 MHz/mm
t	0.91 MHz/mm

The evaluation of the RF parameters in a five cell structure has been

performed with the model shown in Fig. 2.5.

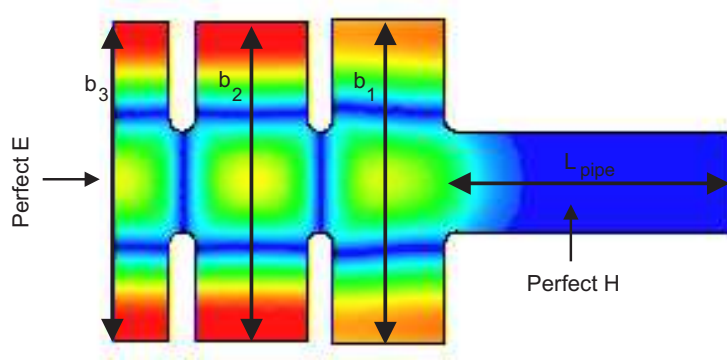


Figure 2.5: *Magnetic field amplitude in the HFSS model used to evaluate the field flatness.*

Setting all the external radii to b , a non-uniform magnetic field profile has been observed on axes, thus we varied b_1 to improve the field flatness. Moving the external radius from $b_1 = 57.64$ to $b_1 = 58.24$ we achieved, with reference to the normalized transversal magnetic field $H_{t,n}$, the flatness $F = 7\%$, as is shown in Fig. 2.6.

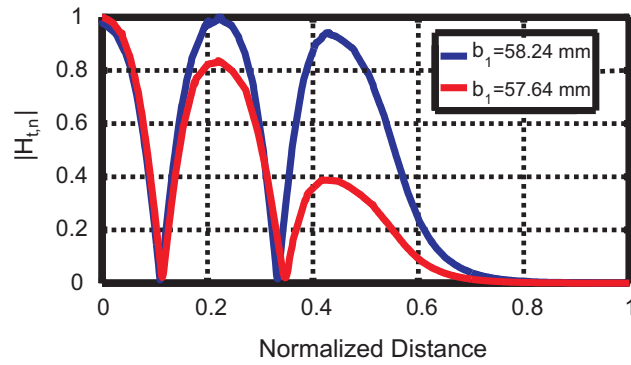


Figure 2.6: *Normalized magnetic field amplitude on axis for different values of the external radius R_1 .*

The model in Fig. 2.5 has also been used to obtain the resonant frequencies of the five cell structure. If the boundary condition in the half of the middle cell is that of a perfect electric conductor, only the modes which are excitable by the coupler (π , $\frac{1}{5}\pi$ and $\frac{3}{5}\pi$) can be found. The other resonant modes ($\frac{4}{5}\pi$ and $\frac{2}{5}\pi$) have been obtained using a perfect magnetic conductor as

a boundary condition in the half of the middle cell. The results are reported in Table 2.2.

Table 2.2: *Modes resonant frequencies obtained with HFSS*

f_π	2.9976 GHz
$f_{\frac{4}{5}\pi}$	3.0045 GHz
$f_{\frac{3}{5}\pi}$	3.0281 GHz
$f_{\frac{2}{5}\pi}$	3.0663 GHz
$f_{\frac{1}{5}\pi}$	3.1090 GHz

The frequency shifts of the nearest modes are $\Delta f_1 = f_{\frac{4}{5}\pi} - f_\pi = 6.9$ MHz and $\Delta f_2 = f_{\frac{3}{5}\pi} - f_\pi = 30.5$ MHz. The excitation of the π -mode has been obtained by simultaneously varying the middle radius b_1 and x_w in the model shown in Fig. 2.7.

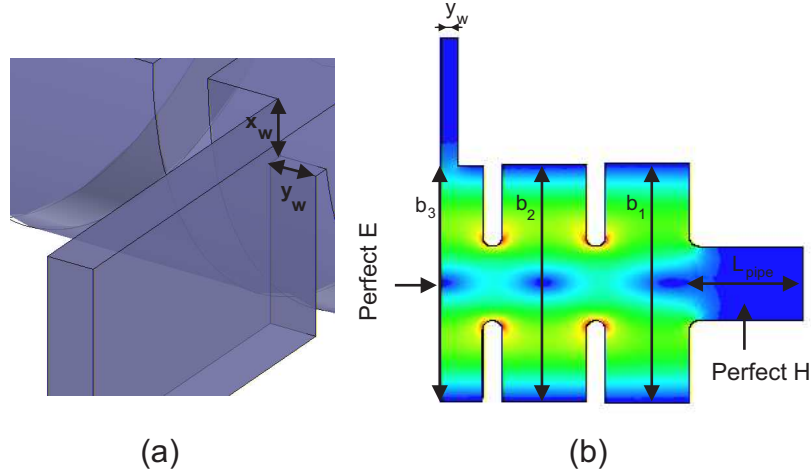


Figure 2.7: (a) *Coupler detail* (b) *Electric field amplitude in the HFSS model used to evaluate the excitation of the deflecting mode.*

Choosing $b_3 = 57.45$ mm and $x_w = 19.5$ mm, and slightly moving b_2 to 57.6 mm and b_3 to 58.25 mm to optimize the coupling, we found a coupling coefficient $\beta = 1.08$ corresponding to a scattering parameter $s_{11} = -27.8$ db. We have evaluated $E_{y,n} = \frac{qE_y}{\max(qcBx/\mu)}$ and $H_{x,n} = \frac{qcBx/\mu}{\max(qcBx/\mu)}$ on z axis in Fig. 2.8.

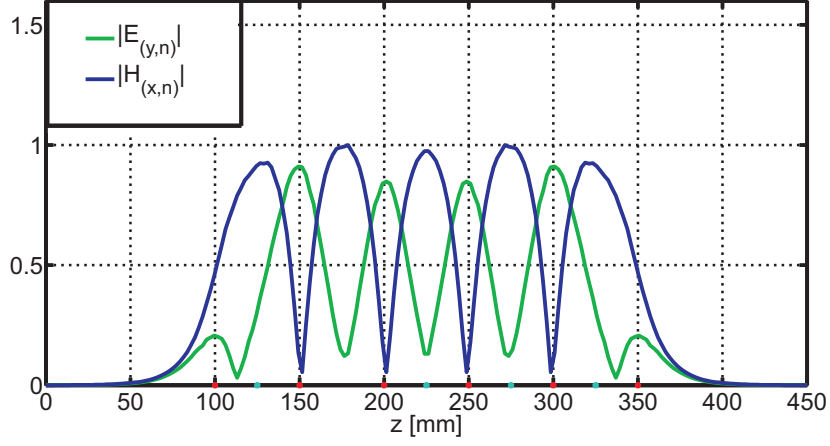


Figure 2.8: $E_{y,n}$ and $H_{x,n}$ evaluated on z axis as a function of the longitudinal deflector coordinate; the red and the blue points on the z axis represent the middle of the iris and the middle of the cells, respectively.

As we can see from Fig. 2.8, the magnetic field contribution in the bunch deflection is slightly larger. The integrated deflecting voltage produced by the cavity is given by:

$$V_t = \sqrt{2P_{in} r_t} \quad (2.1)$$

where the deflecting voltage V_t can be evaluated on the s axis as:

$$|V_t| = \left| \frac{c}{\omega} \int_0^{l_{tot}} \frac{\partial E_z}{\partial s} \Big|_{y=0} e^{j\frac{\omega}{c}s} ds \right| \quad (2.2)$$

The ratio between the shunt resistance and the quality factor is given by:

$$\frac{r_t}{Q} = \frac{|V_t|^2}{2\omega U} \quad (2.3)$$

where U is the total electromagnetic energy of the cavity. Thus the shunt resistance r_t has been calculated using equation (2.3) after evaluating the quality factor Q with the electromagnetic code HFSS. The final geometrical and RF parameters of the five cells structure have been reported in Table 2.3.

Table 2.3: Main RF and geometrical parameters of the low energy deflector.

L_{cell}	50.00 mm	f	2.998 GHz
b_1	58.25 mm	Q_0	15600
b_2	57.60 mm	r_t	2.4 M Ω
b_3	57.45 mm	r_t/Q_0	156 Ω
a	18 mm	t_F	2.4 μ s
y_w	8 mm	$V_t@5$ MW	4.9 MV
x_w	19.5 mm	s_{11}	-27.8 dB
t	9.5 mm	β	1.08

With the maximum input power $P_{in}=5$ MW, an integrated deflecting voltage $V_t=4.9$ MV is achievable. The required deflecting voltage $V_t = 3$ MV can be reached with an input power $P_{in} = 1.9$ MW if the pulse width is greater than $t_F=2.4$ μ s. In these conditions we obtain, for the maximum electric peak, $E_p = 48$ MV/m.

As it will be discussed in section 3.1, during the operations performed with the deflector, the maximum obtained value of input power has been $P_{in} = 1.4$ MW with an attenuation of 7 dB, corresponding to a deflecting voltage $V_t=2.03$ MV. In fact, due to the absence of the circulator in the deflector arm, some instabilities in the vacuum level of the RF gun arm were observed increasing the input power. With the insertion of the circulator (which will be done during the first months of 2011), the cavity will be able to operate at the design value of $V_t=3$ MV.

2.3 Bead-pull measurements

The low energy deflector has been realized and brazed at INFN/LNF workshops, where the first RF measurements with the network analyzer have been done. Then the cavity has been installed in FERMI@Elettra project in December 2009, where further tests and the final tuning were performed; the room temperature was 20.7°C. Fig. 2.9 shows the transmission coefficient between two pick-ups placed in the two external cells. The five observed

resonances are reported in Table 2.4.

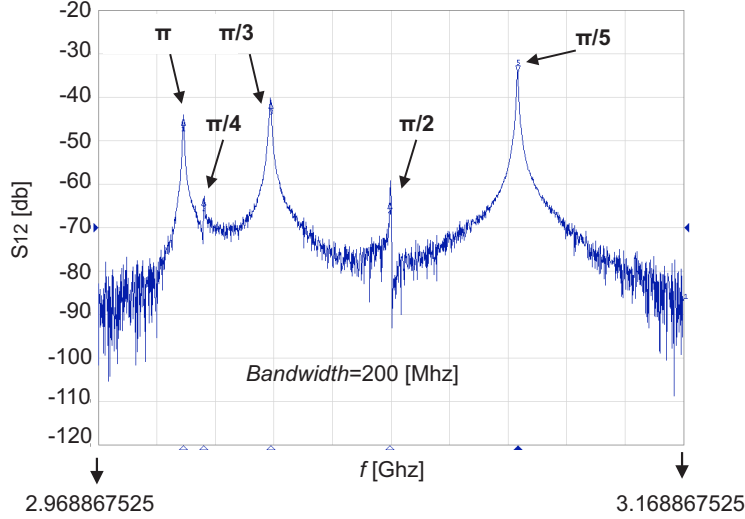


Figure 2.9: Resonant modes in the low energy deflector.

Table 2.4: Modes resonant frequencies measured with the network analyzer.

$f_{r,\pi}$	2.99802 GHz
$f_{r,\frac{4}{5}\pi}$	3.00492 GHz
$f_{r,\frac{3}{5}\pi}$	3.02773 GHz
$f_{r,\frac{2}{5}\pi}$	3.06856 GHz
$f_{r,\frac{1}{5}\pi}$	3.11219 GHz

The frequency shifts $\Delta f_{r,1} = f_{r,\frac{4}{5}\pi} - f_{r,\pi} = 6.9$ MHz and $\Delta f_{r,2} = f_{r,\frac{3}{5}\pi} - f_{r,\pi} = 29.7$ MHz have approximately the same values of Δf_1 and Δf_2 , which have been predicted by HFSS. We measured the load quality factor Q_l of the deflecting mode by evaluating the s_{12} transmission coefficient between the input coupler and one pick-up. Then we obtained the coupling coefficient β by measuring the s_{11} coefficient from the input coupler. Thus we were able to calculate the unloaded quality factor as $Q_0 = Q_l(1 + \beta)$ and the external quality factor as $Q_{ext} = Q_0/\beta$. The filling time has been calculated

as $t_F = 3\tau$, where $\tau = \frac{2Q_l}{2\pi f}$. The experimental results and the predicted value are reported in Table 2.5.

Table 2.5: Comparison between the RF parameters simulated and measured.

	HFSS	Measured
β	1.08	1.1
Q_0	15600	14600
Q_l	7090	6900
Q_{ext}	14300	13200
$\tau[\mu s]$	0.8	0.74
s_{11}	-27.8	-26.3

We can observe a good agreement between the RF parameters obtained with HFSS and the experimental parameters.

In order to evaluate the field flatness, we used the bead pull technique [15], [16]. Thus we moved a small bead attached to a thin nylon line through the cavity, evaluating the frequency shift of the deflecting mode, which is proportional to the squared local field. In particular, we evaluate the phase $\Delta\phi$ of the coefficient s_{12} , which is proportional to the frequency shift due to the perturbation. The measurement was first performed with a metallic sphere, which perturbs both the electric and the magnetic field. Then we used a dielectric cylinder, which affects only the electric field. Since in the middle of the iris the magnetic field is zero, the perturbation introduced by the metallic sphere is completely given by the electric field. For this reason the two traces can be normalized using the maximum value of $\Delta\phi$ in the middle of the iris. Subtracting the squares of the normalized traces we obtained the results shown in Fig. 2.10; the field flatness achieved is $F = 6\%$.

After testing field flatness, the cavity was finally tuned to the working frequency $f=2.998.01$ GHz in vacuum, using the cooling system and the tuners.

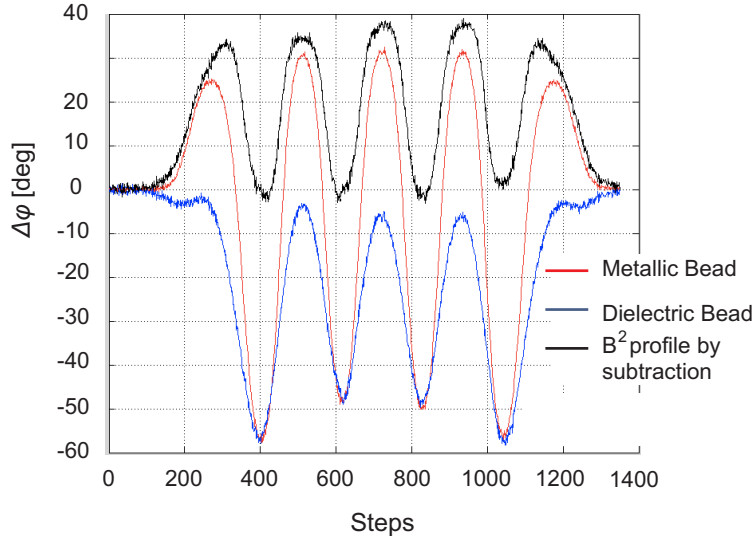


Figure 2.10: *Flatness field obtained with bead pull measurements.*

2.4 Bunch compressor

In the FERMI@Elettra Project the bunch compressor BC1 is located after the accelerating section linac 1, at 350 MeV. As discussed in section 1.1, the booster linac accelerating section increases the beam energy up to $E_0=100$ MeV, while the remaining energy $E_1=250$ MeV is provided by linac 1. The compression scheme exploits a beam energy reduction, which can be obtained by changing the RF phase φ_{L1RF} in the accelerating section linac 1. In fact, the total beam energy E at the end of the bunch compressor is given by:

$$E = E_0 + E_1 \cos \varphi_{L1RF} \quad (2.4)$$

where, in our case $E_0=100$ MeV, and $E_1=250$ MeV. When the bunch compressor is off, $\varphi_{RF} = 0$ and the bunch is accelerated "on crest" in linac 1 and reaches its maximum energy. When the bunch compressor is on, $\varphi_{RF} = \bar{\varphi}_{RF}$ (usually $\bar{\varphi}_{RF} < 30$ deg), and the total beam energy decreases. In this case, an energy modulation is applied to the bunch. In particular, the head and the tail have a lower energy with respect to the bunch center.

Fig.2.11 shows a schematic layout of the magnetic chicane, which is com-

posed by four dipoles. The bunch compressor is designed in such a way that, due to the energy modulation, the electrons travel with different trajectories inside the magnetic dipole chicane, and this results in an overall bunch compression and in an increase of the peak current. In the compression scheme the quadrupoles simply control the beam focalization.

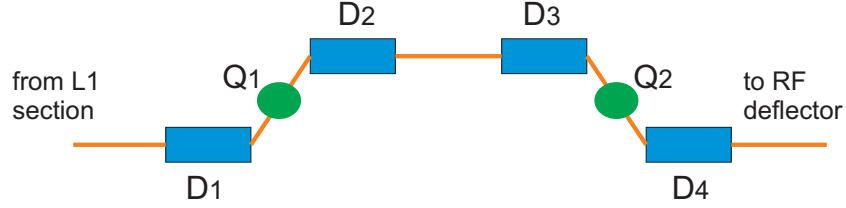


Figure 2.11: *Schematic layout of the magnetic chicane of BC1; D_i (with $i = 1, 2, 3, 4$) are the magnetostatic dipoles while Q_1 and Q_2 are magnetostatic quadrupoles.*

2.5 Optical layout

The optics in the BC1 area is reported in [17] and has been performed with Elegant software [18]. The optical design must satisfy many constraints; in particular it must take into account the bunch compressor and the radio-frequency deflector. Regarding the latter, the parameter $R_{34} = \sqrt{\bar{\beta}_{y,S}\bar{\beta}_{y,D}} \sin \Delta\bar{\phi}_{y,DS}$ has to be maximized, where D and S mean the deflector and the screen position, respectively. In fact, increasing R_{34} allows a good resolution at the screen according to:

$$\Delta y_S = R_{34}\Delta y \quad (2.5)$$

which is equation (1.53) referred to the vertical direction. For the bunch compressor efficiency, the optics should minimize the coherent synchrotron radiation emitted in the magnetic chicane, and consequently it avoid a bunch emittance growth. The optics has also to be used to match the Twiss parameters in the BC1 area, which means that the two independent parameters $\bar{\alpha}$ and $\bar{\beta}$ should have the design values in the horizontal and in the vertical direction [10].

These constraints have led to the optics reported in Fig. 2.12, which is suitable either for beam diagnostic and for beam transport. Four quadrupoles placed in the accelerating section preceding BC1 (linac 1) have been used to excite a high $\bar{\beta}_y = 68$ m in the position in which the deflector has been placed. Downstream of BC1, five quadrupoles over 2.5 m with an average integrated strength of $\bar{Z}=0.18$ m^{-1} build a low-symmetric optics ($\bar{\beta}_x = \bar{\beta}_y$).

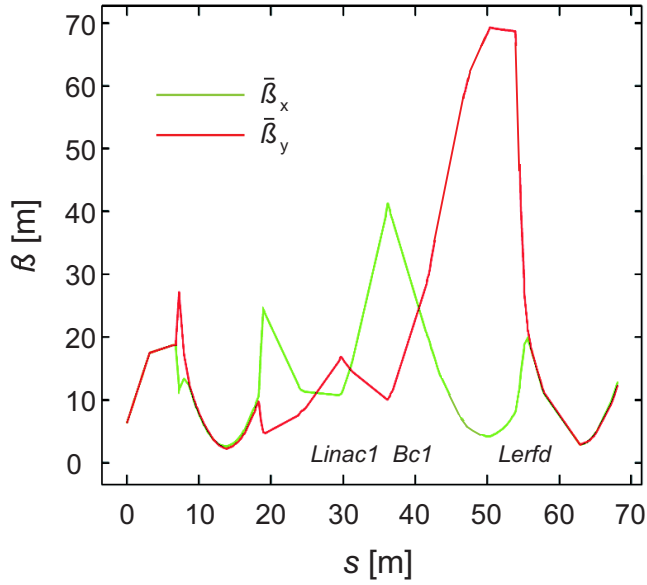


Figure 2.12: *Horizontal and vertical betatron function along the linac, up to the bunch compressor area.*

Four screens have been placed after the deflector, as is shown in Fig. 2.13. Three of them, bc2.ccd, bc3.ccd and bc4.ccd, are placed in the straight line, and can be used for bunch length and emittance slice measurements, while the fourth screen, bcs.ccd, is placed in the spectrometer line. All screens are fabricated using the Yttrium Aluminum Garnet Cerium (YAG) crystal technology [1]. In particular, after the collision with the electron beam, the screen emits light by scintillation, and a lens system brings the light to the couple charge device (CCD) where the light is collected and converted in an image. The bunch images produced by the CCD camera have the vertical size of 11.4 mm and the horizontal size of 15.3 mm, with a resolution of 19.6 μm .

The bunch is vertically deflected, according to the product of the transver-

sal radio-frequency kick of the deflector and to the R_{34} parameter (equation (2.5)). In particular $R_{34}=5\text{m}$, 14m , 22m , from the first to the third screen, respectively. Thus the third screen $bc4.ccd$, having the highest R_{34} value, is the best for the bunch measurement. On the other hand the best choice for the emittance slice measurements is the second screen, where $\bar{\beta}_x = \bar{\beta}_y = 3\text{m}$. In fact in the second screen the vertical dimension on the electron bunch remains constant during a quadrupole-scan, as it will be discussed in section 3.6. Since the second screen provides also a good enlargement of the deflected bunch, it has been used for all the bunch measurements presented in chapter 3.

The BC1 area is completed by the spectrometer, which is a magnetostatic dipole inserted between $bc3.ccd$ and $bc4.ccd$. The spectrometer deflects the beam horizontally in the dispersive line and can be used to measure the energy distribution by means of the screen $bcs.ccd$.

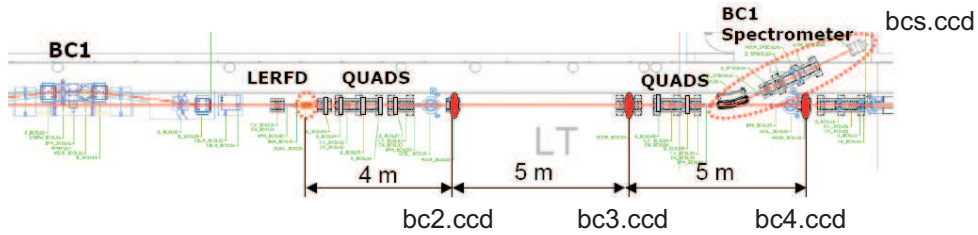


Figure 2.13: Positions of the screens $bc2.ccd$, $bc3.ccd$, $bc4.ccd$ and $bcs.ccd$ in the bunch compressor area.

Chapter 3

Bunch Measurements

3.1 Calibration

The calibration of the radio-frequency deflector is usually done before any other operation with the cavity. During the calibration procedure the phase shifter placed in the deflector arm is moved until the condition of zero crossing is reached, and then an estimation of the deflecting voltage is performed to characterize the cavity behavior. Since the low energy deflector stretches the beam in the vertical plane, the equation of Section 1.6 must be rewritten in the vertical direction. In particular, equations (1.55), (1.59) and (1.62) becomes respectively:

$$\bar{\Delta}y_S = \frac{eV_t}{E} R_{34} \sin \phi_{RF} \quad (3.1)$$

$$z = q \frac{V_t R_{34}}{E_{tot}} k \Delta y_S \quad (3.2)$$

$$\sigma_z = \sqrt{b} \frac{E_{tot}}{qkR_{34}} \quad (3.3)$$

We can note, from equations (3.2) and (3.3), that even supposing to know exactly the deflecting voltage V_t by means of oscilloscope reading, this is not

sufficient to calculate the bunch profile and to evaluate the bunch length σ_z . In fact, the optics, and in particular the R_{34} parameter, may be slightly different from the design value, due to some optical mismatches, which means that for some reasons the bunch is not travelling in the ideal orbit. Furthermore, also the beam energy E_{tot} may be temporally unknown. Hence, the equations of section (1.6) must be rewritten in such a way to simplify the beam measurements with the deflector. For this reason we introduced the calibration coefficient

$$B_{cal} = qR_{34} \frac{V_t}{E_{tot}} \quad (3.4)$$

We can note that, using equations (3.1) and (3.4), the transverse centroid offset at the screen can be written as:

$$\Delta y_S = B_{cal} \sin \phi_{RF} \quad (3.5)$$

Let us note that equation (3.1) and consequently equation (3.5) refer to a beam perfectly aligned to the center of the screen, while in the real case an offset coefficient q has to be taken in account. Furthermore, also the zero-crossing condition will be reached for a given value $\phi_{RF} = \phi_{RF,0}$ of the phase shifter. Thus we generalize equation (3.5) in:

$$\Delta y_S = B_{cal} \sin (\phi_{RF} - \phi_{RF,0}) + q \quad (3.6)$$

From equation (3.6) we can see that, in order to calculate B_{cal} , it is sufficient to vary the phase shifter in a wide range, evaluating Δy_S from the images obtained at the screen, and then to perform a fitting of the experimental data with a *sin* function. As an example of a *sin*-calibration, let us consider the electron bunch shown in Fig. (3.1).

The beam in Fig. (3.1) has been obtained setting the attenuator to 27 dB, and the phase shifter to 0 deg, using the YAG screen of the ccd.03 camera. In this case the attenuation is so high that the deflecting voltage can not be read by the oscilloscope. In fact, the signals are attenuated by the sixty-meters

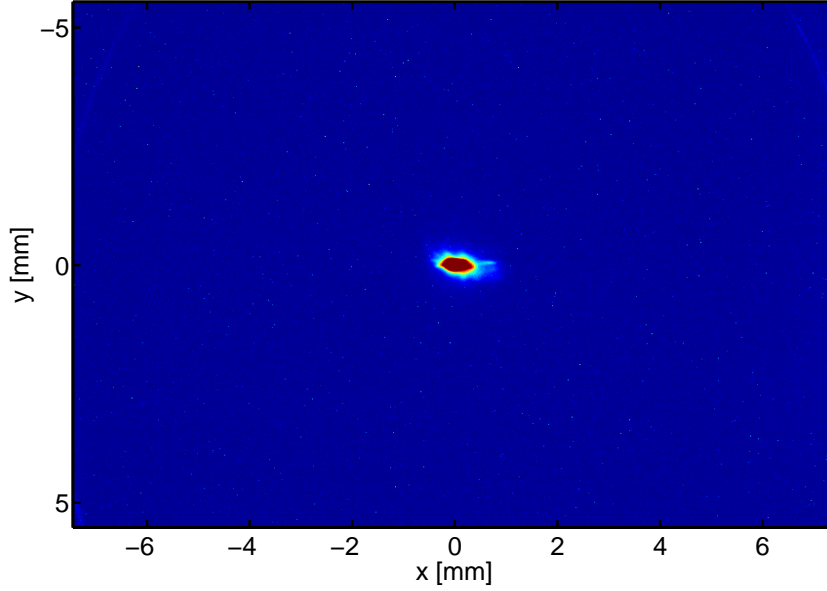


Figure 3.1: *Electron bunch observed at ccd.03 YAG, attenuation 27 dB and $\phi_{RF} = 0$.*

coaxial cable which connects the directional coupler to the oscilloscope. We can only roughly estimate a deflecting voltage $V_t \cong 0.1$ MV.

Moving the phase shifter from 0° deg to 360° deg in 20 steps, and overlapping the images obtained at the screen, we obtained the image in Fig. 3.2.

We can see the typical sin-behavior of Δy_S as a function of ϕ_{RF} . Evaluating the Δy_S at the screen and processing the data we obtained $B_{cal} = 2.7$ mm and $\phi_{RF,0} = 147$ [deg].

However, the *sin*-calibration can be used only for very low deflecting voltage, while we are interested in using higher values of V_t , to increase the instrument resolution. In fact, our goal is to obtain a stretched bunch having a vertical length as long as possible, thus the correlation between the longitudinal coordinate z of the bunch and the vertical coordinate at the screen is maximized. This is the case of the bunch shown in Fig. 3.3, which has been obtained at zero crossing with an attenuation of 12 dB corresponding to $V_t=1.13$ MV.

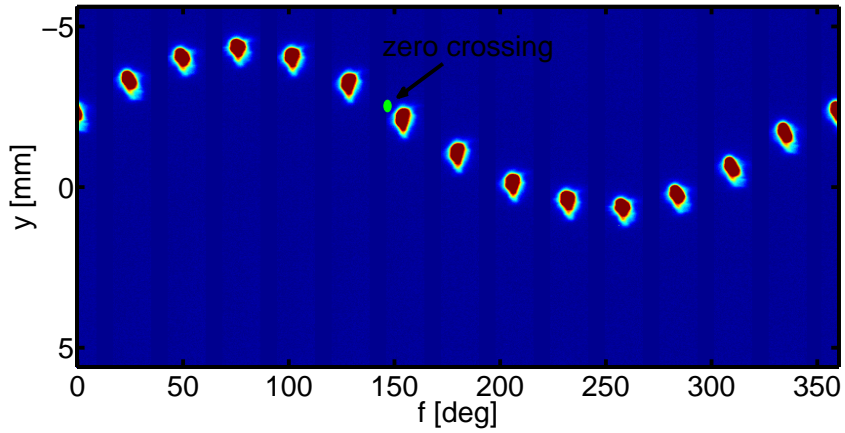


Figure 3.2: Bunches observed at *ccd.03* YAG, attenuation 27 dB and ϕ_{RF} varying from 0° deg to 360° in 20 steps.

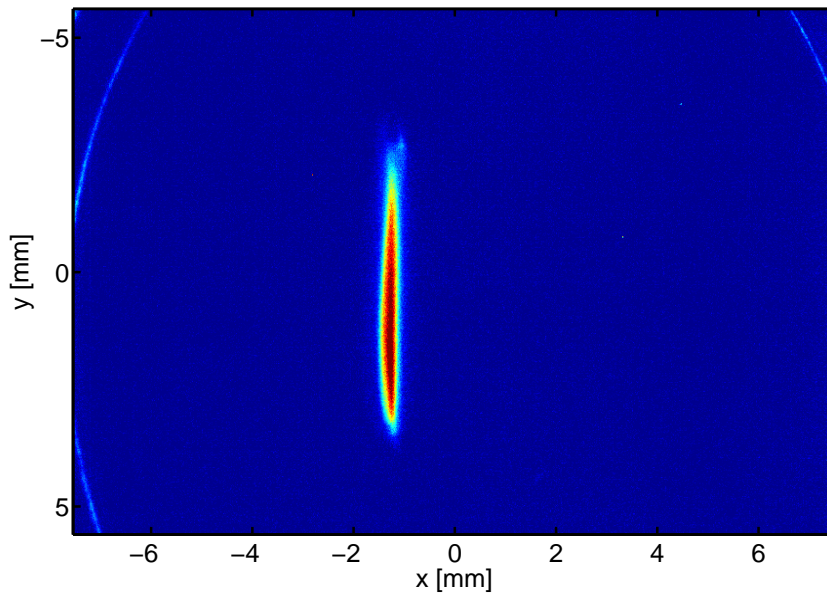


Figure 3.3: Bunch observed at *ccd.03* YAG, attenuation 12 dB, $V_t=1.13$ MV.

Since the deflecting voltage is high, it is not possible to perform a *sin*-calibration with the electron bunch in Fig. 3.3. In fact, in these conditions the bunch would go outside of the screen when moving the phase shifter from 0 deg to 360 deg. For this reason we have used another method to calibrate

the instrument. From equation (3.6) we can note that B_{cal} can be evaluated as

$$B_{cal} = \left. \frac{\partial \Delta y_S}{\partial \phi_{RF}} \right|_{\phi_{RF} = \phi_{RF,0}} \quad (3.7)$$

Thus B_{cal} can be evaluated as the slope of the *sin*-function at zero crossing. In a standard calibration, once the zero crossing has been obtained, the phase shifter is moved up and down of few degrees on the screen, as is shown in Fig. 3.4. In this way B_{cal} can be calculated with equation (3.7) by simply evaluating the centroid of images and taking into account the range in which the phase shifter is moved.

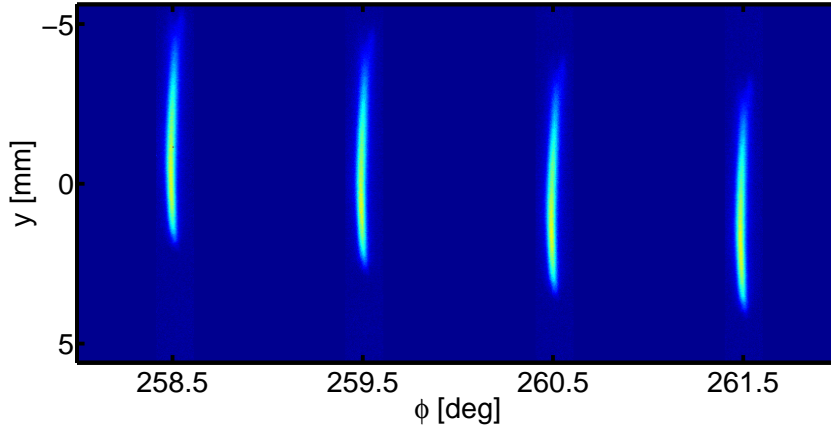


Figure 3.4: Calibration at *ccd.03* YAG, attenuation 12 dB, $V_t=1.13$ MV the phase shifter is moved from 258.5 deg to 261.5 deg in four steps.

Before performing the first bunch measurements in the FERMI@Elettra control room, our original plan for calibrating the low-energy radio-frequency deflector was that of using the *sin*-calibration with a low deflecting voltage to find the zero crossing, subsequently increasing the deflecting voltage and obtaining other calibration factors B_{cal} with the slope-method. However for high deflecting voltages a quicker approach has been adopted to find the zero-crossing condition, and in particular we have used the two beam position monitors (BPM) placed before and after the deflector. The BPM are radio-frequency cavities capable of reading the transversal position of the

bunch centroid [19]. Since, by equation (1.57), in the zero crossing condition the bunch centroid does not change its transversal position, the zero-crossing condition can be easily obtained varying the values of the phase shifter of the deflector arm and observing for which value the two BPM give the same reading.

3.2 Bunch length measurement

In this section we describe the first two bunch length measurements performed in October 2010. The first measurement has been performed with an uncompressed bunch, while the second one with a compressed bunch obtained by turning on the bunch compressor with $\varphi_{L1RF} = 25$ deg. For the uncompressed bunch the beam energy was $E=350.3$ MeV, thus for the compressed bunch the beam energy becomes $E=326.8$ MeV according to equation (2.4). The bunch charge extracted was 250 pC.

The uncompressed bunch is represented in Fig. 3.3 of the previous section, and it has been obtained stretching the beam with an attenuation of 12 dB, corresponding to $V_t=1.13$ MV. Fig. 3.5 shows a screen shot of the compressed bunch, which has been obtained with an attenuation of 7 dB, corresponding to $V_t=2.01$ MV.

We have shown in Fig 3.6 the vertical projection for both the uncompressed and the compressed bunches. We can see that, with the bunch compressor "on", the beam shape becomes triangular from parabolic. This implies an increase of the peak current, as will be discussed in Section 3.3.

According to equations (1.61) and (1.62) of Section 1, an estimate of the bunch length can be obtained with the parabolic fitting, considering at least two different deflecting voltages. For the uncompressed bunch we have adopted an attenuation of 12 dB, while for the compressed bunch we have used an attenuation of 7 dB. In both case we have first acquired a set of images at zero crossing condition, and then we have moved the phase shifter of phase 180 deg, that is the π -crossing condition. In fact with this procedure we acquire image at $+V_t$ and $-V_t$, respectively. In order to perform the parabolic fitting we have used also a third point low voltage point, setting in both cases the attenuation at 28 dB. The calibration results are reported in Table

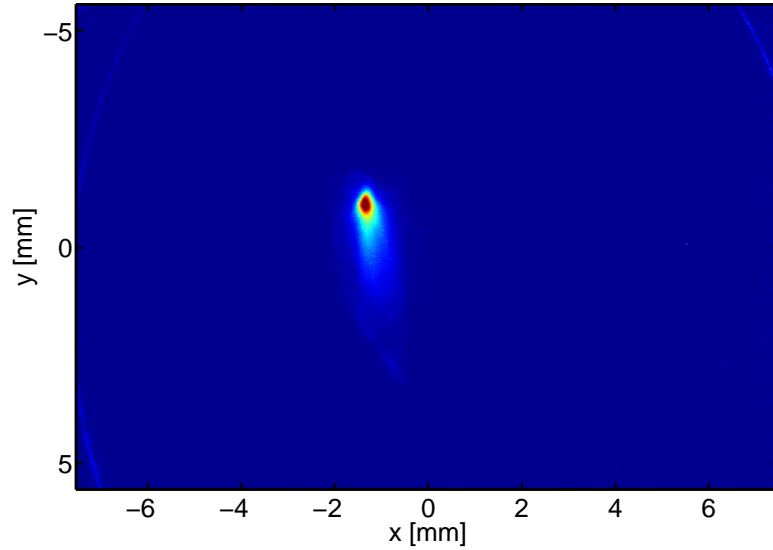


Figure 3.5: *Screen shot of the compressed bunch stretched with the attenuator at 7 dB, $V_t=2.01$ MV.*

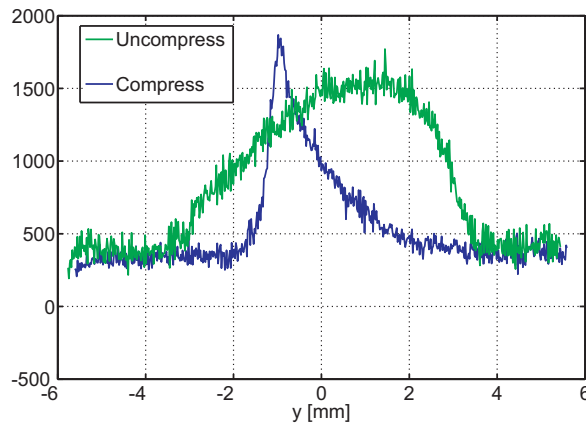


Figure 3.6: *Vertical projection on the screen for both the uncompressed and the compressed bunches. The vertical axis is dimensionless.*

3.1, where the subscripts nc and c mean 'not-compressed' and 'compressed', respectively, and the subscripts 1, 2 and 3 mean 'zero-crossing condition', ' π -crossing condition' and 'low-deflecting voltage', respectively.

The values listed in Table 3.1 have been used to estimate the beam optics,

Table 3.1: Calibration of the deflector.

$B_{1,nc}$ [mm]	41.5
$B_{2,nc}$ [mm]	-46.5
$B_{3,nc}$ [mm]	2.39
$B_{1,c}$ [mm]	-86.1
$B_{2,c}$ [mm]	93.1
$B_{3,c}$ [mm]	2.22

in particular the R_{34} value. We have first calculated the absolute mean values of the calibration factors corresponding to the highest deflecting voltages, thus finding $\bar{B}_{nc}=44.0$ mm for the uncompressed bunch and $\bar{B}_c=89.6$ mm for the compressed bunch. The beam energy and the deflecting voltage, in the two cases have the values $E_{tot}=350.3$ MeV and 336.8 MeV, and $V_t=1.13$ MV and 2.01 MV, respectively. With these data we have calculated the R_{34} parameter with equation (3.5), finding $R_{34}=13.6$ m for the uncompressed bunch and $R_{34}=15$ m for the compressed. Such values are both near to the optical design value $R_{34}=14$ m. Thus the low energy deflector, together with the energy spectrometer and the diodes setup for the input power evaluation, has been used to perform an indirect measurement of the beam optics, which has confirmed the design value with good accuracy.

Using equation (1.62) we obtain, for the standard deviation of the bunch length, the values $\sigma_{z,nc}=552$ μm and $\sigma_{z,c}=127$ μm , for the uncompressed and the compressed case, respectively, and the bunch results to be compressed in σ_z approximately by a factor 4. The parabolic fitting plot is shown in Fig. 3.7.

3.3 Profile reconstruction

Using the calibration factor of equation (3.4) in (3.2), we can observe that the vertical position of the bunch on the screen y is related to the longitudinal coordinate z by:

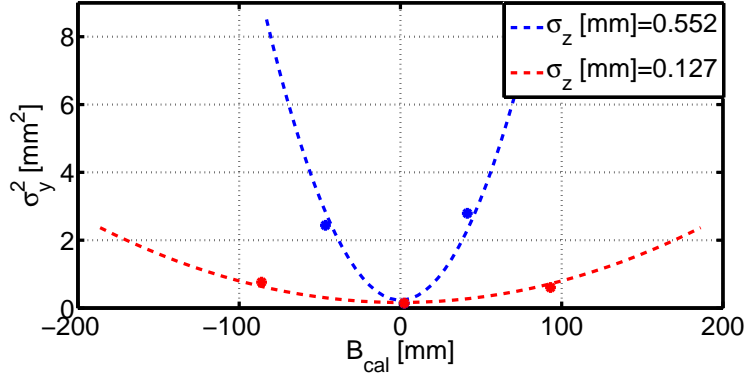


Figure 3.7: *Parabolic fitting for the uncompressed and the compressed bunch: the dots represent the experimental data, while the dashed lines represent the fitting.*

$$y = B_{cal}kz \quad (3.8)$$

Thus, projecting the images obtained on the screens on the vertical axis y and using equation (3.8) is possible to reconstruct the longitudinal beam profile. We can note that if the total beam charge is known, also the beam current can be evaluated using the reconstructed profile.

We have performed the longitudinal profile analysis for the compressed and uncompressed bunches considered in Sections 3.1 and 3.2. Furthermore we have analyzed the intermediate-compressed bunch represented in Fig. 3.8.

The intermediate-compressed bunch and the compressed bunch have been obtained in November 2010 using $V_t=1.79$ MV (8 dB attenuation) with the same setting of the dipoles D_i of the bunch compressor, but varying the quadrupole strength. In particular, for the intermediate-compressed bunch we have increased the focalization of the quadrupole Q_1 and Q_2 inside BC1, thus minimizing the distance between the different particles paths in the magnetic chicane. Since the bunch compression in BC1 is due to the different particle paths, increasing the quadrupole focalization reduces the bunch compressor efficiency: for this reason we refer to this bunch as an intermediate-compressed bunch.

With reference to the intermediate-compressed bunch and the compressed

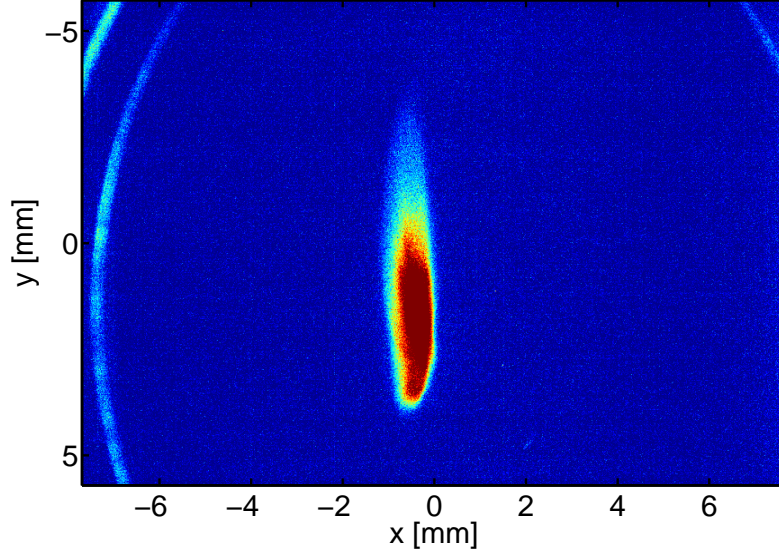


Figure 3.8: Screen shot of the intermediate compressed bunch stretched with the attenuator at 8 dB, $V_t=1.79$ MV.

bunch, the calibration factors are reported in Table 3.2, where the subscripts ic and c mean 'intermediate-compressed' and 'compressed', respectively, and the subscripts 1, 2 denote 'zero-crossing condition', and ' π -crossing condition', respectively.

Table 3.2: Calibration factor of the deflectors

$B_{1,ic}$ [mm]	70.6
$B_{2,ic}$ [mm]	-72.1
$B_{1,c}$ [mm]	70.4
$B_{2,c}$ [mm]	-73.0

The absolute mean values of the calibration factors are $\bar{B}_{ic}=71.3$ mm and $\bar{B}_c=71.7$ mm for the intermediate compressed bunch and the compressed bunch, respectively. Thus, as it was expected, the calibration factor was approximately the same for both measurements, since the optics and the deflecting voltage in the bunch compressor area were not changed. The decrease of \bar{B}_c with respect to October 2010 can be partially explained with

the lower deflecting voltage used, but we can not exclude a slight change in the machine optics which provides different operating conditions.

We show in Fig. 3.9 eight consecutive profiles captured at the screen for the compressed bunch.

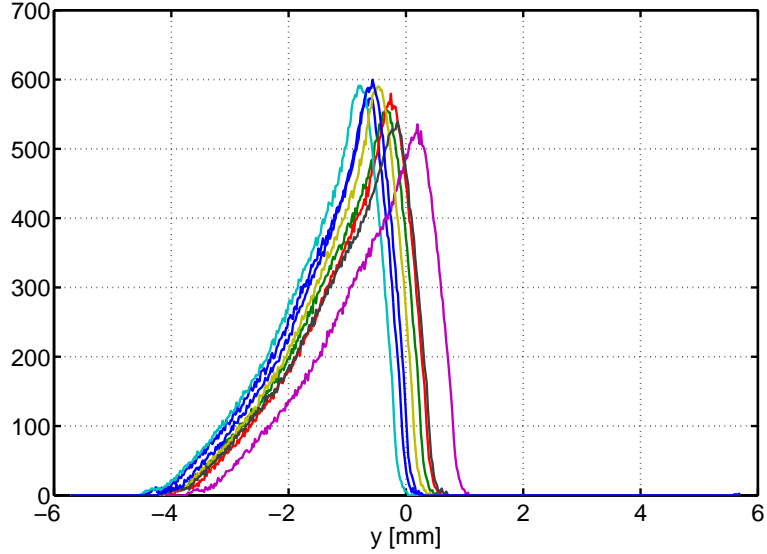


Figure 3.9: *Eight consecutive vertical projections captured at the ccd.03 screen.*

We can see as the bunch slides from the left to the right of Fig. 3.9. This beam instability has been observed and monitored during the FERMI@Elettra commissioning, and thus was present also during the deflector measurements. While changing its position on the screen, the beam changes also its shape. For this reason in our analysis we first aligned the profile obtained, and then we evaluated an average profile. Taking into account that the beam charge extracted by the RF-gun was $Q = 250$ pC, we show in Fig. 3.10 the current profiles obtained.

We can see from Fig. 3.10 that the bunch profile changes during the process of compression. In particular the uncompressed bunch has a parabolic profile, while the compressed one has a triangular shape. For this reason the beam peak current in the compressed bunch is by a factor 2.5 higher than the peak current corresponding to the uncompressed bunch. In particular,

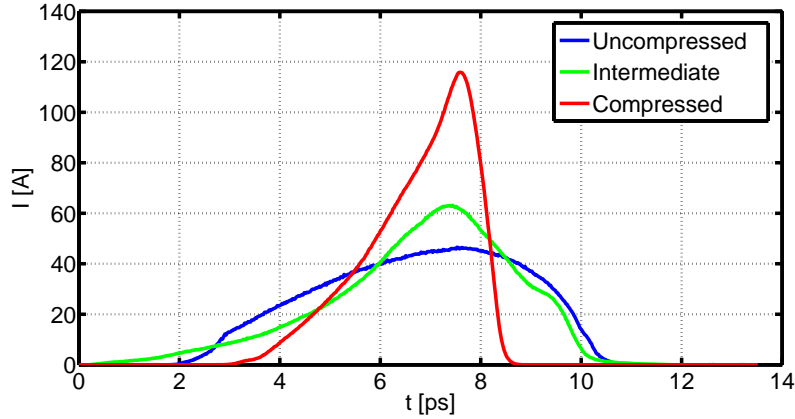


Figure 3.10: *Current Profiles for the uncompressed, intermediate-compressed and compressed bunch.*

the peak current increases from $I=46.5$ A to $I=115.8$ A turning "on" the bunch compressor. From Fig. 3.10 we can also observe that the intermediate bunch, obtained increasing the focalization of the bunch compressor quadrupoles, has an intermediate shape between the uncompressed and the compressed bunch, due to decrease of the bunch compressor efficiency in that operating condition.

Table 3.3 reports the full-width half-maximum values (FWHM) of the three considered bunches. We can observe, in the compressed bunch, a reduction of approximately a factor 5 in the FWHM with respect to the uncompressed bunch.

Table 3.3: *Full-width half-maximum values*

	Uncompressed	Intermediate-Compressed	Compressed
FWHM [ps]	5.7	2.1	1.1

3.4 Instrument resolution

The instrument resolution is essentially given by the bunch transversal finite dimension of the beam [20]. As described in section 1.6 (see equation (1.60)),

the beam trace observed on the screen consists of two parts, one depending on the deflecting voltage and the other on the finite dimension of the beam. Considering a vertical deflector and setting $\sigma_{y,S} = \nu\sigma_{y,0}$, equation (1.60) can be written as

$$\sigma_{y,S,R} = \sigma_{y,S} \frac{\sqrt{1 + \nu^2}}{\nu} \quad (3.9)$$

Thus we can define the resolution error, due to the finite dimension of the beam, as

$$e_{rel,R} = \frac{\sigma_{y,S,R} - \sigma_{y,S}}{\sigma_{y,S}} \quad (3.10)$$

which by means of equation (3.9) can be written in the form:

$$e_{rel,0} = \left| \frac{\sqrt{1 + \nu^2}}{\nu} - 1 \right| \quad (3.11)$$

The resolution error $e_{rel,0}$ in equation (3.11) is shown in Fig. 3.11.

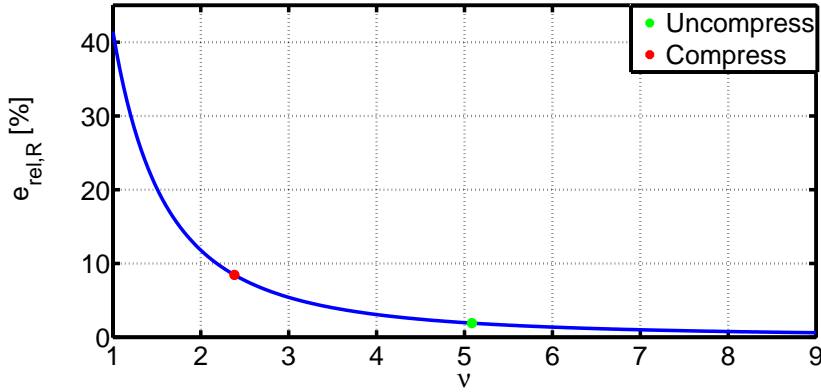


Figure 3.11: Relative error on the bunch length measurement as a function of ν .

In a bunch length measurement, the resolution error can be avoided in the σ_z calculation, since equations (1.61) and (1.62) take into account the finite dimension of the beam. On the other hand the resolution error persists

in the profile reconstruction, which is obtained by equation (3.8). In order to estimate the resolution error, we can first obtain $\sigma_{y,S}$ with:

$$\sigma_{y,S} = \sigma_z B_{cal} k \quad (3.12)$$

Using equation (3.12) we have estimated $\sigma_{y,S}=1.5$ mm and $\sigma_{y,S}=0.73$ mm for the uncompressed bunch and the compressed bunch, respectively. The beam dimensions observed at the screen with the deflector "off" were $\sigma_{y,0}=0.3$ mm, from which we can obtain $\nu=5.1$ and $\nu=2.4$, which correspond to $e_{rel,0}=2\%$ and $e_{rel,0}=8\%$, for the uncompressed and the compressed bunch, respectively (Fig. 3.11).

3.5 Quadrupole scan

The quadrupole scan is a technique to measure the beam emittance and the optical parameters of an electron distribution. Measuring the beam size of the electron distribution on the screen, as a function of the quadrupole field strength \bar{Z} , it is possible to recover the Twiss parameters ($\beta_{e,x}, \alpha_{e,x}, \gamma_{e,x}$) and the emittance ε_x [21]. Considering the quadrupole matrix of equation (1.44), and the matrix

$$S_x = \begin{pmatrix} S_{11} & S_{12} \\ S_{21} & S_{22} \end{pmatrix} \quad (3.13)$$

which describes the path from the quadrupole to the screen, the total transfer matrix is given by

$$S_x R_x = \begin{pmatrix} S_{11} + \bar{Z} S_{12} & S_{12} \\ S_{12} + \bar{Z} S_{22} & S_{22} \end{pmatrix} \quad (3.14)$$

The beam matrix of equation (1.33) can be written at the input section of the quadrupole as

$$\bar{\sigma}_{x,0} = \begin{pmatrix} \Sigma_{11_0} & \Sigma_{12_0} \\ \Sigma_{12_0} & \Sigma_{22_0} \end{pmatrix} \quad (3.15)$$

where we have placed $\Sigma_{11_0} = \langle x^2 \rangle$, $\Sigma_{22_0} = \langle x'^2 \rangle$ and $\Sigma_{12_0} = \langle x x' \rangle$. Thus the beam matrix at the screen is given by equation (1.39):

$$\bar{\sigma}_{x,S} = \begin{pmatrix} \Sigma_{11_S} & \Sigma_{12_S} \\ \Sigma_{12_S} & \Sigma_{22_S} \end{pmatrix} = (S_x R_x) \bar{\sigma}_0 (S_x R_x)^T \quad (3.16)$$

Let us note that the element $\Sigma_{11_S} = \langle x^2 \rangle$ of equation (3.16) can be obtained observing the bunch images at the screen. $\Sigma_{11_S} = \langle x^2 \rangle$ is related to the quadrupole integrated field strength \bar{Z} , to the matrix S_x and to the beam matrix elements as follow:

$$\begin{aligned} \Sigma_{11_S} = & (S_{11}^2 \Sigma_{11_0} + 2 S_{11} S_{12} \Sigma_{12_0} + S_{12}^2 \Sigma_{22_0}) + \\ & + (2 S_{11} S_{12} \Sigma_{11_0} + S_{12}^2 \Sigma_{22_0}) \bar{Z} + S_{12}^2 \Sigma_{11_0} \bar{Z}^2 \end{aligned} \quad (3.17)$$

which can be written as

$$\Sigma_{11_S} = A \bar{Z}^2 - 2AB \bar{Z} + (C + AB^2) \quad (3.18)$$

where:

$$\begin{cases} A = S_{12}^2 \Sigma_{11_0} \\ -2AB = 2S_{11} S_{12} \Sigma_{11_0} + 2S_{12}^2 \Sigma_{12_0} \\ C + AB = S_{11}^2 \Sigma_{11_0} + 2S_{11} S_{12} \Sigma_{12_0} + S_{12}^2 \Sigma_{22_0} \end{cases} \quad (3.19)$$

Let us note that since the matrix S is known, the quadrupole strength is known, and for each value of \bar{Z} a value of Σ_{11_S} can be measured. Thus using three (or more) different values of \bar{Z} it is possible to obtain A , $-2AB$ and $C + AB$ with a parabolic fitting (see equation (3.18)). Hence also the value of A , B and C can be calculated. From equation (3.19) we can obtain, for the elements of the beam matrix, the expressions:

$$\begin{cases} \Sigma_{11_0} = \frac{A}{S_{12}^2} \\ \Sigma_{12_0} = -\frac{A}{S_{12}^2} \left(B + \frac{S_{11}}{S_{12}} \right) \\ \Sigma_{22_0} = \frac{1}{S_{12}^2} \left[(AB^2 + C) + 2AB \left(\frac{S_{11}}{S_{12}} \right) + A \left(\frac{S_{11}}{S_{12}} \right)^2 \right] \end{cases} \quad (3.20)$$

Hence the emittance can be recovered by means of equation (1.37):

$$\varepsilon_x = \sqrt{\det \bar{\sigma}_{x,S}} = \sqrt{\Sigma_{11S} \Sigma_{22S} - \Sigma_{12S}^2} \quad (3.21)$$

from which

$$\varepsilon_x = \frac{\sqrt{AC}}{S_{12}^2} \quad (3.22)$$

The Twiss parameters can be calculated with:

$$\begin{cases} \bar{\beta}_{e,x} = \sqrt{\frac{A}{C}} \\ \bar{\alpha}_{e,x} = \sqrt{\frac{A}{C}} \left(B + \frac{S_{11}}{S_{12}} \right) \\ \bar{\gamma}_{e,x} = \frac{S_{12}^2}{\sqrt{AC}} \left[(AB^2 + C) + 2AB \left(\frac{S_{11}}{S_{12}} \right) + A \left(\frac{S_{11}}{S_{12}} \right)^2 \right] \end{cases} \quad (3.23)$$

3.6 Emittance measurement

In the FERMI@Elettra linear accelerator, the emittance measurements with the quadrupole scan technique can be done in three points of the machine, located after the booster linac accelerating section, in the bunch compressor area and at the end of linac 4.

In this section we report a typical emittance measurement performed in the bunch compressor area, in order to describe the operations which have been also used in the emittance slice measurements. As we have described in section 2.5, five quadrupoles have been placed after the low-energy radio frequency deflector. During the normal operations, the quadrupole focalization and defocalization is provided varying the current I , which is related to the quadrupole strength \bar{Z} by the relation:

$$\bar{Z} = \frac{0.2997}{E_{tot}[GeV]} \bar{l} C I \quad (3.24)$$

where \bar{l} is the quadrupole length and C is the quadrupole calibration factor, so that $C I$ represents the quadrupole gradient [11]. During a typical

quadrupole scan in the bunch compressor area, the first four quadrupole were set to the nominal currents values, which drive the beam in the design orbit. On the other hand, the last quadrupole was employed with different current settings, which were used to perform the parabolic fit of equation (3.18) evaluating the standard deviation Σ_{11_S} of the bunch collided to the screen. We note that in our experimental setup, the S_x matrix is simply a drift, thus is described by equation (1.40). Hence $S_{11}=S_{22}=1$, $S_{21}=0$ and $S_{12}=l_D$, where $l_D=6.5$ m for the screen bc3.ccd.

We report in Fig. 3.12 some electron bunches observed during an horizontal emittance measurement performed on a compressed beam, varying the last quadrupole current from $I=0$ A to $I=6$ A in nine steps. The beam energy was $E_{tot}=325.8$ MeV and the total charge $Q=250$ pC.

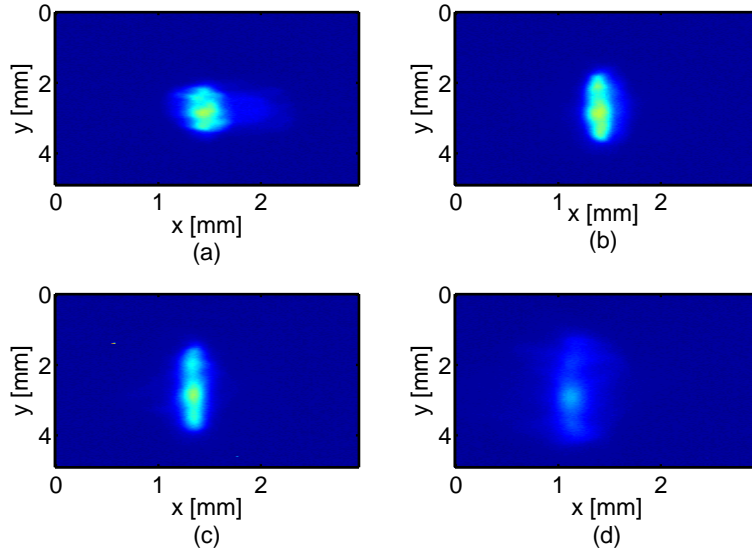


Figure 3.12: *Bunches observed during an horizontal emittance measurement at bc3.ccd screen: (a) $I=0$ A, (b) $I=2.25$ A, (c) $I=3.75$ A, (d) $I=6$ A.*

Since in the horizontal emittance measurements we are interested in the calculation of the horizontal standard deviation at the screen, we can set $\sigma_x = \Sigma_{11_S}$. Fig. 3.13 shows the parabolic fitting obtained on the experimental data. For the horizontal emittance we obtained $\epsilon_x=1.8$ mm mrad.

We note from Fig. 3.13 that the current variation of the fifth quadrupole

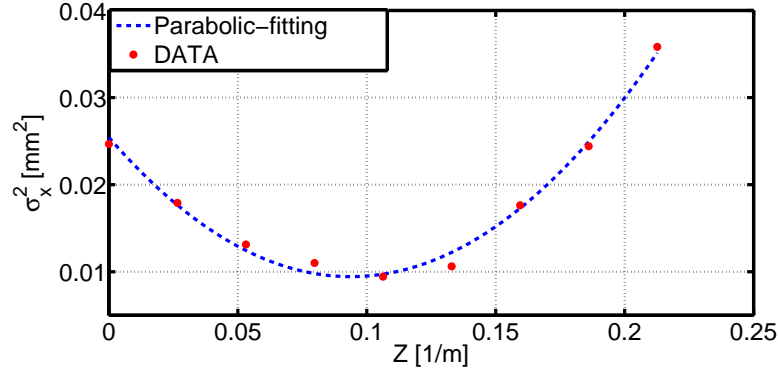


Figure 3.13: *Parabolic fitting of σ_x as a function of \bar{Z} for a compressed bunch having $E_{tot}=325.8$ MeV and $Q=250$ pC.*

has been chosen to obtain a minimum in σ_x . This can be observed also from Fig. 3.12, where we can see that the bunch images corresponding to $I=2.25$ A and $I=3.75$ A are more focalized in the horizontal direction.

3.7 Emittance slice measurement

The quadrupole-scan technique can be applied also to a deflected bunch, using the linear correlation between the vertical screen coordinate y and the longitudinal bunch coordinate z described by equation (3.8). Thus the quadrupole-scan with the deflector "on" provides a measurement of the horizontal slice emittance and the Twiss parameters along the longitudinal bunch coordinate z . Note that with a vertical deflector only the horizontal slice emittance can be evaluated: in order to evaluate the vertical slice emittance an horizontal deflector should be used.

We report in Fig. 3.14 some bunch images observed during an horizontal slice emittance measurement performed on the uncompressed beam of Fig. 3.3, varying the last quadrupole current from $I=-6$ A to $I=2$ A in nine steps. The beam energy was $E_{tot}=349.8$ MeV and the total charge $Q=250$ pC.

In an emittance slice measurement, each bunch image acquired, such that shown in Fig. 3.14, must be divided in a proper number of slices. The number of slices must be equal or lower than the resolution ratio ν between

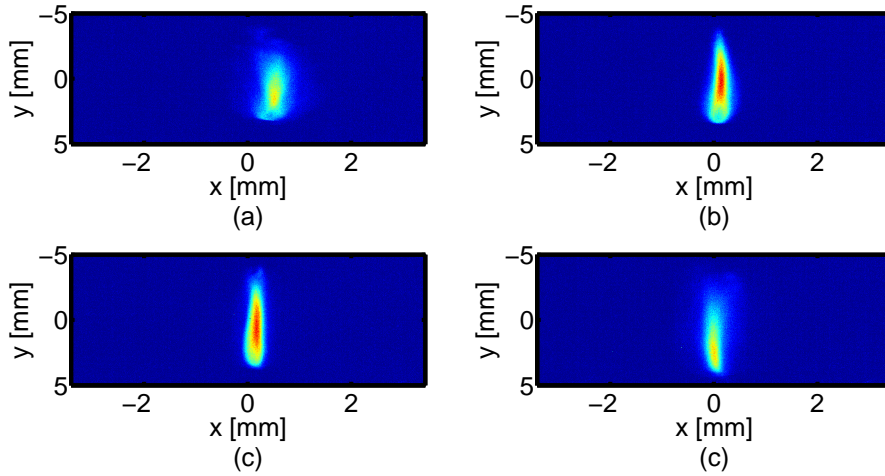


Figure 3.14: *Bunches observed during an horizontal slice emittance measurement at the bc3.ccd screen: (a) $I=-6$ A, (b) $I=-3$ A, (c) $I=0$, (d) $I=2$ A.*

the vertical length of the deflected and undeflected bunch: in this case we have analyzed five slices. As an example, we have reported in Fig. 3.15 the slices decomposition of the bunch image in Fig. 3.14 (c).

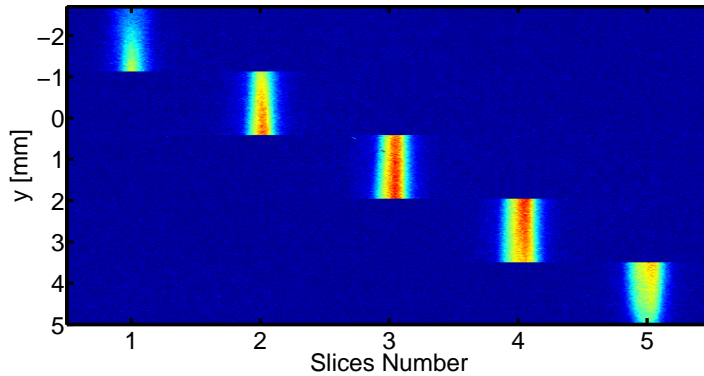


Figure 3.15: *Slice decomposition of the uncompressed bunch: the first and the fifth slice are the bunch tail and the bunch head, respectively.*

The optics in the second screen is designed in order to minimize the variation of the bunch vertical trace during a quadrupole scan. However, a slight difference in the vertical dimension persists, as is shown in Fig. 3.14. This must be taken in account in the slice decomposition, thus a

simple algorithm which detects the beginning and the end of the vertical trace of the electron bunch at the screen has been developed. In this way the quadrupole-scan theory of section 3.6 can be applied to every slice, and the slice emittance can be evaluated performing a parabolic fitting: the results are plotted in Fig. 3.16.

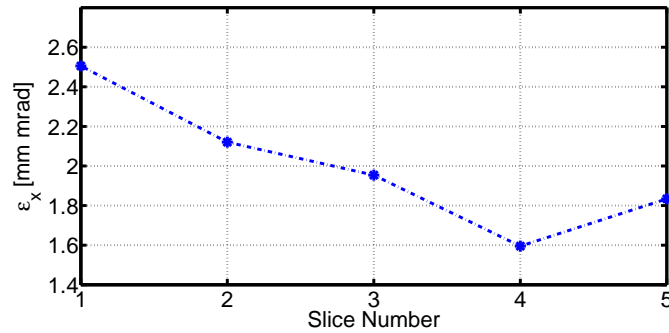


Figure 3.16: *Horizontal emittance as a function of the slice number for an uncompressed bunch.*

We can see that the emittance increases from the head to the tail of the bunch. We have reported in Fig. 3.17 the horizontal betatron function for every slice, which has been evaluated by equation (3.23).

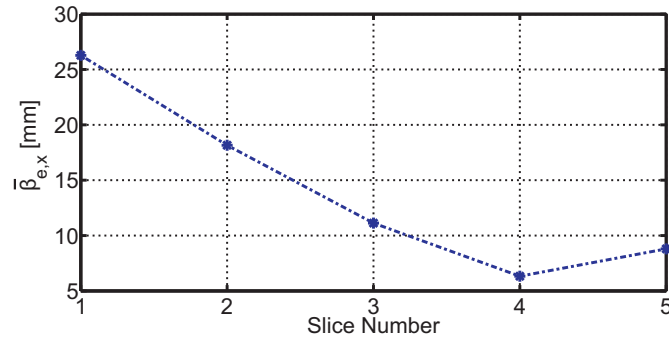


Figure 3.17: *Horizontal betatron function as a function of the slice number for an uncompressed bunch.*

From Fig. 3.17 we can see that also the horizontal betatron function increases from the head to the tail of the bunch. Since the betatron function is related to the beam motion by means of equation (1.24), the measurement

suggests that the tail of the bunch is subjected to a wider oscillation in the betatron motion. The emittance growth from the head to the tail of the bunch can be due to the transversal wakefield effect produced by the linear accelerator before the bunch compressor. In fact, as it will be described in Section 5, the transversal wakefield effect is induced to the tail of the bunch from the head of the bunch, producing an instability effect which is related to the emittance growth [22].

Chapter 4

High Energy Deflectors

4.1 Technical specifications

The high energy deflectors of the FERMI@Elettra Project will operate at the end of the main linac, just before the undulator chains. The two cavities will be identical, but one will deflect the beam in the vertical plane, and the other in the horizontal plane. In this way the deflectors will completely characterize the beam properties at the input section of the FEL lines, in particular measuring the bunch length and the slice emittance in both planes. The main constraints of the high energy deflectors have been reported in Table 4.1 [20]:

Table 4.1: *Main RF and geometrical constraints of the high energy deflector.*

f	2.998 GHz
V_t	20 MV
t_F	3 μ s
P_{in}	15 MW
l_{tot}	2.5 m

The working frequency f is that assigned for the FERMI@Elettra Project. The required deflecting voltage of $V_t=20$ MV is obtainable with the maximum available input power $P_{in}=15$ MW, which travels in rectangular pulses having

a maximum duration of $4.5 \mu\text{s}$ and a repetition rate from 10 Hz to 50 Hz. The available space is $l_{tot}=2.5$ m. These constraints can be satisfied with a travelling wave structure, which will be described in the following sections.

4.2 Group velocity derivation

For a travelling wave deflector, equations (1.13) and (1.14) can be used to calculate the power flux of the electromagnetic field using the Poynting vector, obtaining:

$$P = \frac{1}{2} \int_S \text{Re} \{E \times H^*\} dS = \pi a^2 \frac{E_0}{2Z_0} \left(\frac{ka}{2}\right)^2 \left[\frac{4}{3} \left(\frac{ka}{2}\right)^2 - 1 \right] \quad (4.1)$$

as reported in [23], [24]. We can see from equation (4.1) that the Poynting vector flux is positive $ka > \sqrt{3}$ and negative if $ka < \sqrt{3}$. A closed form for the group velocity as a function of the iris radius can be found in [25], [26], which use the model in Fig. 4.1.

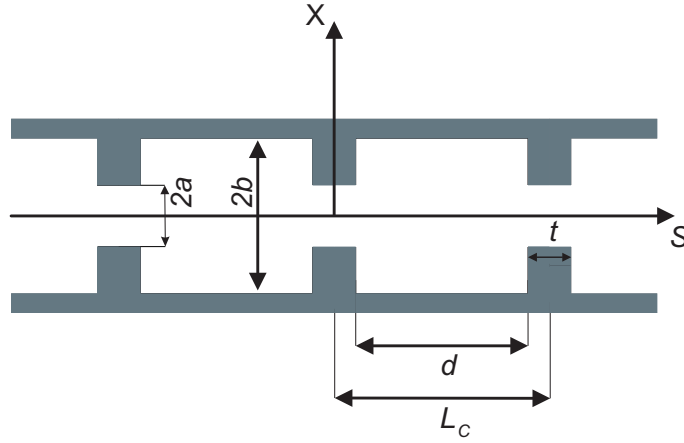


Figure 4.1: Geometrical model for the group velocity calculations.

Defining the parameters $d = L_c - t$ (which takes into account the disk thickness) and $\xi = \frac{d}{L}$, it can be shown that the dispersion relationship of the fundamental harmonic, synchronous at the speed of light, is given by:

$$\frac{\varphi_1(ka, kb)}{\varphi_0(ka, kb)} - \xi \frac{ka}{2} + \frac{1}{ka} (\xi - 1) = 0 \quad (4.2)$$

where:

$$\varphi_0(ka, kb) = J_1(kb) I_1(ka) - I_1(kb) J_1(ka)$$

and

$$\varphi_1(ka, kb) = J_1(kb) I_2(ka) - I_1(kb) J_2(ka)$$

where $J_m(x)$ is the Bessel function of first kind of order m and $I_m(x)$ is the modified Bessel function of first kind and order m . Equation (4.2) is the relationship between the iris radius a , the external radius b and the wave number k ; it can be used as an example to calculate b once a and k are assigned.

Since $k = \frac{\omega}{c}$, differentiating equation (4.2) with respect to ω is possible to obtain a closed form for the group velocity v_g . Introducing the normalized group velocity $\beta_g = \frac{v_g}{c}$ it can be shown [26] that:

$$\beta_g = \frac{A}{A + B} \quad (4.3)$$

where:

$$A = \xi \left[\frac{(ka)^2}{3} - 1 \right]$$

and

$$B = \left[\zeta + (1 + \zeta) \frac{2}{(ka)^2} \right]^2 \frac{2}{\pi^2 \varphi_1^2(ka, kb)} - 2\zeta^2 \left(\frac{ka}{2} - \frac{1}{ka} \right)^2 + 2(\zeta - 1) + \frac{2}{(ka)^2}$$

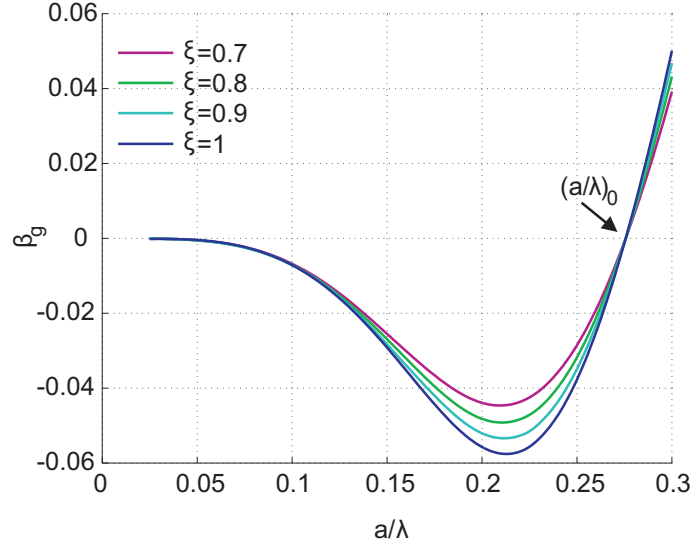


Figure 4.2: β_g as a function of $\frac{a}{\lambda}$, obtained using $\xi = 0.7, 0.8, 0.9, 1.0$.

in which ka e kb must satisfy relation (4.2). Fig. (4.2) shows β_g as a function of $\frac{a}{\lambda}$ for different values of ξ : the plot holds for every value of the working frequency.

From Fig. (4.2) we can observe that in the radio-frequency deflector the group velocity switches from positive to negative values for different values of a ; the intersection at $\beta_g = 0$ does not depend on the disk thickness. We can also notice that $|\beta_g|$ increases for the high values of ξ .

4.3 Shunt resistance and deflecting voltage

The shunt resistance per unit length for a travelling wave deflector is defined as the ratio between the square of the deflecting voltage per unit length and the power dissipated per unit length:

$$r_t = \frac{V_{t,l}^2}{-dP/dz} \quad \left[\frac{\Omega}{m} \right] \quad (4.4)$$

where the deflecting voltage per unit length is defined as $V_{t,l} = \frac{V_t}{l_{tot}}$, thus for equation (1.49)

$$V_{t,l} = \frac{F_x}{q} \quad (4.5)$$

Since by equation (1.15) $F_x = qE_0$, using equation (4.5) the shunt resistance for a travelling wave deflecting mode becomes:

$$r_t = \frac{[E_0]^2}{-\frac{dP}{dz}} \left[\frac{\Omega}{m} \right] \quad (4.6)$$

The quality factor of a travelling wave mode can be defined as:

$$Q = \omega \frac{U_l}{-\frac{dP}{dz}} \quad (4.7)$$

where U_l is the electromagnetic energy per unit length. Since $P = U_l v_g$, from equation (4.7) we obtain:

$$\frac{dP}{dz} = -\frac{\omega P(z)}{Q v_g} \quad (4.8)$$

From equation (4.8) we obtain

$$P(z) = P_0 e^{-2\alpha z} \quad (4.9)$$

which represents the power attenuation inside a travelling wave structure. In equation (4.9) we have defined the attenuation factor as:

$$\alpha = \frac{\omega}{2Q v_g} \quad (4.10)$$

Inserting the attenuation factor in the longitudinal electric field of equation (1.13) and in equation (4.1), we obtain, respectively,

$$E_z(z) = E_0 k x e^{-\alpha z} \quad (4.11)$$

and

$$P_z(z) = \pi a^2 \frac{E_0^2}{2Z_0} \left(\frac{ka}{2}\right)^2 \left[\frac{4}{3} \left(\frac{ka}{2}\right)^2 - 1 \right] e^{-2\alpha z} \quad (4.12)$$

Substituting (4.11) and (4.12) into (4.4), we obtain

$$r_t = \frac{Z_0}{\alpha \pi a^2 \left(\frac{ka}{2}\right)^2 \left[\frac{4}{3} \left(\frac{ka}{2}\right)^2 - 1 \right]} \quad (4.13)$$

which is the theoretical expression of the shunt resistance of the travelling wave deflecting mode. Using (4.10) the $\frac{r_t}{Q}$ ratio can be obtained:

$$\frac{r_t}{Q} = \frac{2Z_0 v_g}{\omega \pi a^2 (ka/2)^2 \left[\frac{4}{3} (ka/2)^2 - 1 \right]} \quad (4.14)$$

which is a closed form expression, since the group velocity v_g can be calculated by equation (4.3). Equation (4.14) has been plotted in Fig. 4.3 using the data $f = 2.998$ GHz, $t = 2, 6, 10$ mm and varying the iris radius a from 1 cm to 4 cm with a step of 5 mm.

We can observe that the highest values of $\frac{r_t}{Q}$ are obtained for the smallest values of the iris radius a and t . Furthermore, from equation (4.4) we can obtain, for the integrated deflecting voltage, the expression:

$$V_t = \int_0^l \sqrt{-r_t \frac{dP}{dz}} dz. \quad (4.15)$$

which using (4.9) becomes:

$$V_t = \sqrt{2\alpha} \frac{(1 - e^{-\alpha l})}{\alpha} \sqrt{P_0 r_t} \quad (4.16)$$

Equation (4.16) can be written as:

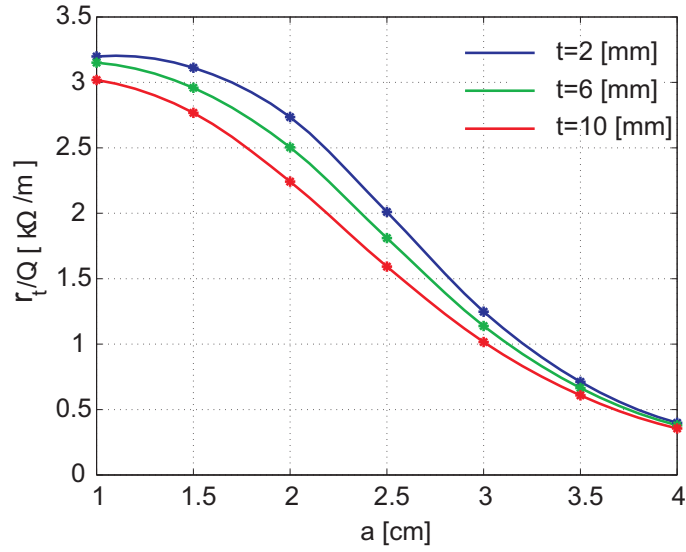


Figure 4.3: Shunt resistance as a function of the iris radius a at $f=2.998\text{GHz}$ for different values of the disk thickness t .

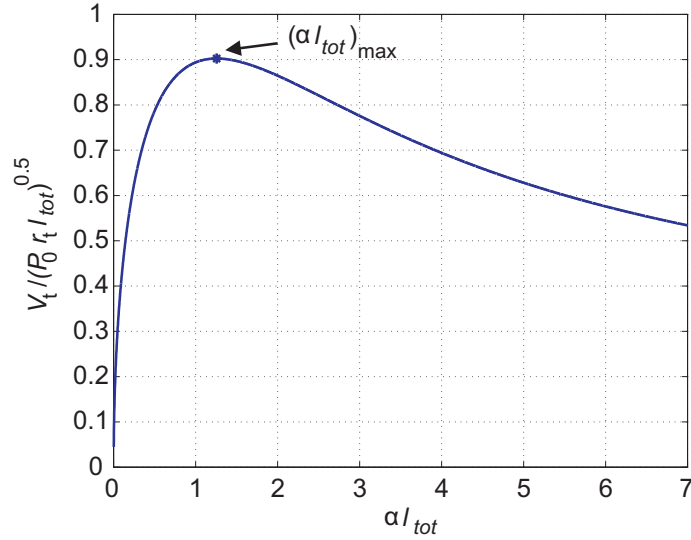


Figure 4.4: $\frac{V_t}{\sqrt{P_0 r_t l_{tot}}}$ as a function of αl .

$$V_t = \sqrt{2\alpha l} \left(\frac{1 - e^{-\alpha l}}{\alpha l} \right) \sqrt{P_0 l r_t} \quad (4.17)$$

We have plotted $\frac{V_t}{\sqrt{P_0 r_t l_{tot}}}$ in Fig 4.4: we can see that the maximum value of V_t is obtained for $\alpha l_{tot} = 1.26$ and is $V_{t,max} = 0.903 q \sqrt{P_0 r_t l_{tot}}$.

We have represented the deflecting voltage V_t of equation (4.16) in Fig. 4.5, as a function of the iris radius a and for different values of l_{tot} . We have set $f=2.998$ GHz and a $Q=10000$; we can see that the highest values of V_t are reached for the smallest values of the iris radius. For this reason the radius of $a=12.5$ [mm] has been chosen in the final design [27].

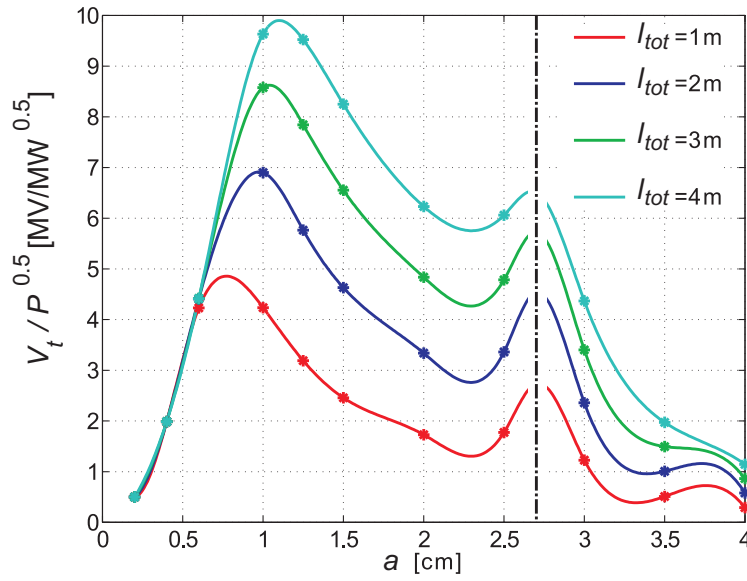


Figure 4.5: Normalized deflecting voltage as function of the iris radius, for different values of the total length l_{tot} . The dash-dotted black vertical line represents an asymptote, and the corresponding iris value cannot be used in the deflector design.

We must remark that the theory above exposed is valid only for the fundamental harmonic of the deflecting mode. In the real case, the total field is composed by all the harmonics, each harmonic dissipates power inside the cavity. For this reason the theoretical description is valid only approximately. However, it has been employed as the basis of the radio-frequency design reported in the following sections. Such design has been carried out with the aid of the electromagnetic code HFSS [14].

4.4 Basic cell design

The starting point of the design of the RF high energy deflector has been the basic cell, represented in Fig. 4.6, where PEC and PMC denote perfect electric and magnetic conductors, respectively, and ϕ is the periodic field phase advance.

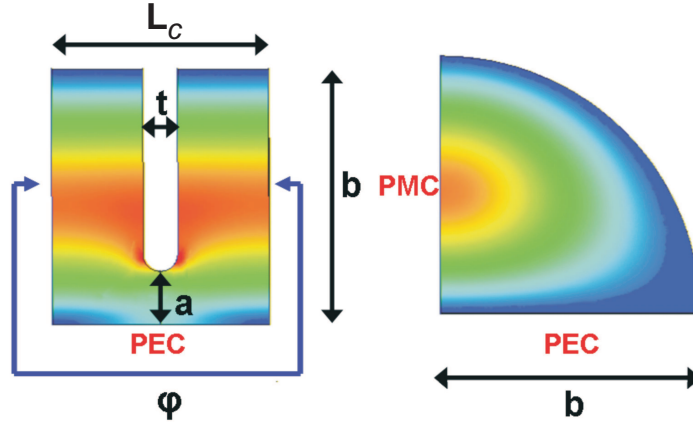


Figure 4.6: A quarter of the basic cell of the high energy deflector.

As shown in section 4.3, equation (4.17) has a maximum in $(\alpha l_{tot})_{OPT} = 1.26$, which is the point of maximum deflecting efficiency. Since in our case the deflector length is determined by the space constraint, to reach this value we can only increase the attenuation constant α . This can be done by reducing the group velocity v_g of the mode, according to equation (4.10). However, since the filling in a travelling wave structure is given by

$$t_F = l_{tot}/v_g \quad (4.18)$$

an excessive group velocity reduction must be avoided in order to satisfy the t_F constraint in Table 4.1. A simple way to decrease the group velocity in a periodic structure is to consider different values of the phase advance ϕ [28]. Let us remark that, since the theory exposed in sections 4.2 and 4.3 holds for the fundamental harmonic of the deflecting field, it can be used for each periodic phase advance ϕ .

The first choice for the phase advance was $\phi = (2/3)\pi$, which has been also considered also at the Stanford Linear Accelerator Center (SLAC) in early 60's when the deflectors were used as particle separators [24]. We have reported in Table 4.2 the geometrical and RF parameters obtained with HFSS. With this option 61 cells are needed in order to achieve 20MV, thus the deflector length would be $l_{tot}=2.04\text{m}$.

Table 4.2: *Main RF and geometrical parameters for the $(2/3)\pi$ mode.*

L_c	33.33 mm	t_f	0.43 μs
b	59.33 mm	r_t	29.9 $M\Omega$
a	12.5 mm	r_t/Q	2.21 $k\Omega$
t	8 mm	α	0.147 1/m
l_{tot}	2.04 m	β_g	0.0157
Q	13500	αl_{tot}	0.30 m

With the $(5/6)\pi$ phase advance choice, the group velocity reduces of 57% with respect to the $(2/3)\pi$ mode and we need 42 cells to achieve 20MV. In this case the deflector should be 1.75m long. Geometrical and RF parameters are reported in Table 4.3.

Table 4.3: *Main RF and geometrical parameters for the $(5/6)\pi$ mode.*

L_c	41.66 mm	t_f	0.66 μs
b	59.52 mm	r_t	29.4 $M\Omega$
a	12.5 mm	r_t/Q	1.86 $k\Omega$
t	8 mm	α	0.222 1/m
l_{tot}	1.75 m	β_g	0.0089
Q	15800	αl_{tot}	0.39 m

Let us consider now a $(17/18)\pi$ phase advance: in this case the group velocity is 20% of the $(2/3)\pi$ mode, but the filling time is still acceptable. Geometrical and RF parameters are reported in Table 4.4; we need 29 cells to satisfy the V_t constraint, and the deflector is 1.37m long.

Table 4.4: *Main RF and geometrical parameters for the $(17/18)\pi$ mode.*

L_c	47.22 mm	t_f	1.48 μs
b	59.66 mm	r_t	26.6 $M\Omega$
a	12.5 mm	r_t/Q	1.55 $k\Omega$
t	8 mm	α	0.594 1/m
l_{tot}	1.37 m	β_g	0.00308
Q	17200	αl_{tot}	0.81 m

In our analysis we have also considered other two phase advances value smaller than $(2/3)\pi$: the $\pi/3$ mode and the $\pi/2$ mode: the results are shown in Tables 4.5 and 4.6. The $\pi/3$ mode and the $\pi/2$ mode need 134 cells and 85 cells to satisfy the deflecting voltage constraints, respectively. For both modes the total length l_{tot} required is greater compared to that obtained with the $(2/3)\pi$ mode, even if the $\pi/2$ mode has a similar performance with respect to the $(2/3)\pi$ mode.

Table 4.5: *Main RF and geometrical parameters for the $\pi/3$ mode.*

L_c	16.66 mm	t_f	0.41 μs
b	59.00 mm	r_t	19.8 $M\Omega$
a	12.5 mm	r_t/Q	2.6 $k\Omega$
t	8 mm	α	0.216 1/m
l_{tot}	2.34 m	β_g	0.0191
Q	7600	αl_{tot}	0.50 m

In order to compare the traveling wave modes, the mode efficiency ζ_ϕ can be introduced as:

$$\zeta_\phi = \frac{V_t(\alpha l_{tot})}{V_t(\alpha l_{tot})_{OPT}} \quad (4.19)$$

As an example, for $\phi = (2/3)\pi$, $(5/6)\pi$ and $(17/18)\pi$ we obtained $\zeta = 0.74$, 0.81 and 0.97, respectively. Thus, reducing the group velocity in the traveling

Table 4.6: *Main RF and geometrical parameters for the $\pi/2$ mode.*

L_c	25 mm	t_f	$0.38\mu\text{s}$
b	59.10 mm	r_t	$25.9 M\Omega$
a	12.5 mm	r_t/Q	$2.4 k\Omega$
t	8 mm	α	0.159 1/m
l_{tot}	2.12 m	β_g	0.0186
Q	10600	αl_{tot}	0.40 m

wave option we have almost reached the maximum deflecting efficiency (Fig. 4.7).

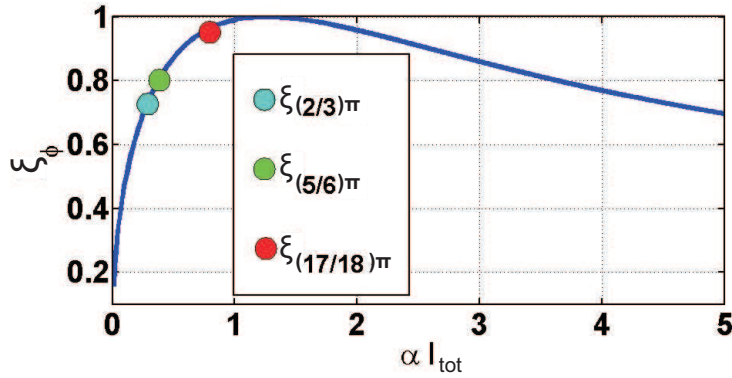


Figure 4.7: *Mode efficiency for different values of the periodic phase advance ϕ .*

The disadvantage of an excessive reduction of the group velocity can be understood observing Figure 4.8, where the dispersion diagram of three modes is shown.

We can see that, for the $(5/6)\pi$ and $(17/18)\pi$ modes, a small variation in the operating frequency, due (for instance) to an error in the basic cell mechanical realization, results in a great difference in the electromagnetic field phase advances. Since (as it will be described in section 4.5) a perturbation in the design phase advance is related to a decrease of the deflector efficiency, the $(2/3)\pi$ mode with the RF and geometrical parameters reported in Table 4.2 has been chosen as the operating mode. In fact, even if the $(2/3)\pi$ mode

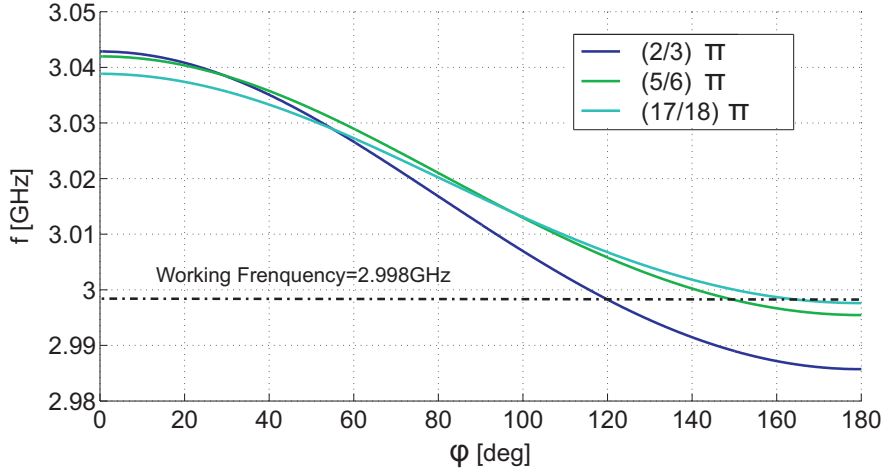


Figure 4.8: Dispersion diagram of the $(2/3)\pi$, $(5/6)\pi$ and $(17/18)\pi$ modes.

has not the same efficiency compared to the $(5/6)\pi$ and $(17/18)\pi$ modes, it is less sensitive to the errors in the basic cell mechanical realization.

The sensitivities of the basic cell of the high energy deflector working in the $(2/3)\pi$ mode are reported in Table 4.7. In the Table, we can observe similar values with respect to the standing wave case reported in Table 2.1. Considering an input power $P_{in}=15$ MW, we obtained for the maximum electric peak $E_p = 23$ MV/m.

Table 4.7: Basic Cell Sensitivities.

a	-16.3 MHz/mm
b	-48.6 MHz/mm
L	2.56 MHz/mm
t	-2.37 MHz/mm

4.5 A detuning error theory

In this section we will describe how a non-optimal electromagnetic field periodicity, due for example to mechanical errors in the realization of the basic

cell, can result in a degradation of the energy exchange between the electromagnetic field and the electron bunches [29]. The starting point of this analysis is the integrated deflecting voltage, which can be expressed as the integral of equation (1.12) along the deflector:

$$V_t = \frac{1}{\beta} \int_{-l_{tot}/2}^{l_{tot}/2} \nabla_t E_z e^{j\omega t} ds \quad (4.20)$$

If we suppose a small perturbation δ_β (>0) in the electromagnetic field phase, the ideal longitudinal electric field of equation (1.16) becomes:

$$E_{p,z} = e_{z,n} e^{\mp j\delta_\beta z} \quad (4.21)$$

Thus, from equations (4.21) and (1.16) we obtain:

$$E_{p,z} = \sum_{n=0}^{\infty} e_{z,n}(T) e^{-j(\beta_0 + \frac{2\pi}{L} n \pm \delta_\beta)z} \quad (4.22)$$

As a consequence, equation (4.20) can be written as:

$$V_{t,p} = \int_{-l_{tot}/2}^{l_{tot}/2} \frac{\nabla_t \sum_{n=0}^{\infty} e_{z,n} e^{-j(\beta_0 + \frac{2\pi}{L} n \pm \delta_\beta)z}}{\beta_0 + \frac{2\pi}{L} n \pm \delta_\beta} e^{j\omega t} dz \quad (4.23)$$

If we consider a particle travelling at the speed of light $\frac{\omega}{c} = \beta_0$, we can write $\omega t = \beta_0 z$. Since for a structure consisting of n cells $l_{tot} = nL_c$, only the first harmonic interacts with the beam, (see Section 1.3). Thus, in the ideal case where $\delta_\beta = 0$, the deflecting voltage reduces to:

$$V_{t,id} = \frac{\nabla_t E_0}{\beta_0} l_{tot} \quad (4.24)$$

Substituting equation (4.24) into equation (4.23), yields:

$$V_{t,p} = V_{t,id} \frac{\beta_0}{l_{tot}} \int_{-l_{tot}/2}^{l_{tot}/2} \frac{e^{\mp j \delta_\beta z}}{\beta_0 \pm \delta_\beta} dz \quad (4.25)$$

Thus, introducing the synchronism factor:

$$A(\delta_\beta) = \frac{1}{l_{tot}} \int_{-l_{tot}/2}^{l_{tot}/2} \frac{\beta_0}{\beta_0 \pm \delta_\beta} e^{\mp j \delta_\beta z} dz \quad (4.26)$$

we can simplify equation (4.25) as follows:

$$V_{t,p} = AV_{t,id} \quad (4.27)$$

Using equations (4.26) and (4.27) we can evaluate the deflecting voltage decrease as a function of the perturbation δ_β . Supposing δ_β as constant, equation (4.26) becomes:

$$A(\delta_\beta) = \frac{\beta}{\beta \pm \delta_\beta} \text{sinc} \left(\frac{\delta_\beta l_{tot}}{2} \right) \quad (4.28)$$

The first zero of (4.28) is given by:

$$\delta_\beta = \left(\frac{2\pi}{L_c} \right) \frac{1}{n} \quad (4.29)$$

thus it depends on the number of cell n . Equation (4.28) has been plotted in Figs. 4.9 and 4.10 considering the deflecting field produced by the basic cell of the $(2/3)\pi$ deflecting mode, thus having $\beta_0 = 62.8$ rad/m. We have set $\Delta\phi_e = \delta_\beta L_c$ with $L_c = 33.33$ mm.

Fig. 4.9 shows that the first zero with respect to $\Delta\phi_e$ becomes smaller when increasing the cell number n . On the other hand, from Fig. 4.9 we can observe that the maximum number of cells satisfying a given synchronism factor $|A|$ increases when decreasing $\Delta\phi_e$.

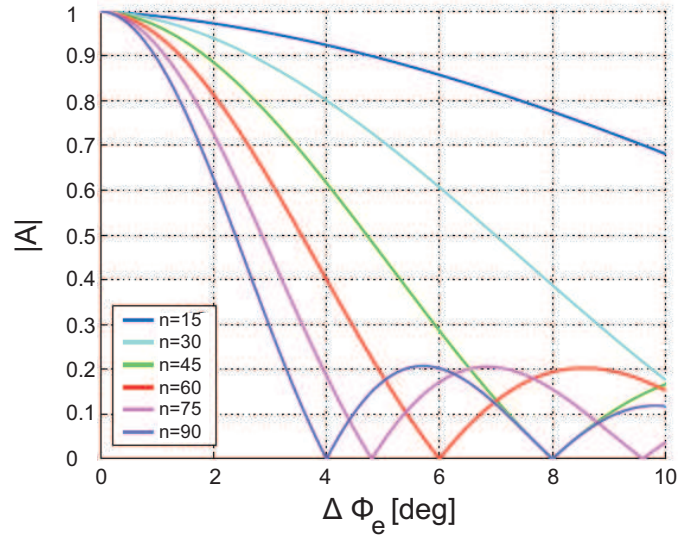


Figure 4.9: $|A|$ as a function of $\Delta\phi_e$ for different values of the cell number n .

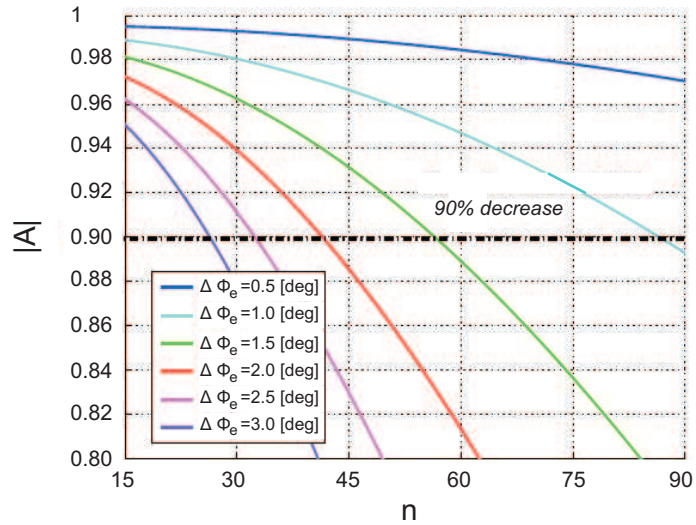


Figure 4.10: $|A|$ as a function of the cell number n for different values of $\Delta\phi_e$.

If we suppose that δ_β is a random variable produced, as an example, by a mechanical realization error of the deflector cell, the synchronism factor of equation (4.28) can be written as:

$$A = \frac{1}{l_{tot}} \sum_{i=0}^{n-1} \int_{-\frac{nL_c}{2} + iL_c}^{-\frac{nL_c}{2} + (i+1)L_c} \frac{\beta}{\beta \pm \delta_\beta} e^{\mp j\delta_{\beta,i}z} dz \quad (4.30)$$

which simplifies in:

$$A = \frac{1}{n} \sum_{i=0}^{n-1} \frac{\beta}{\beta \pm \delta_{\beta,i}} e^{\pm j\delta_{\beta,i}L_c(\frac{n-1}{2}-i)} \text{sinc} \left(\frac{\delta_{\beta,i}L_c}{2} \right) \quad (4.31)$$

Equation (4.31) is useful to evaluate the effect of a random perturbation of the cell, supposing that $\Delta\phi_e$ is a random variable of mean value equal to zero and standard deviation equal to 1 [deg], in accordance to the typical realization errors of the travelling wave disk loaded waveguide. We have reported in Table 4.8 the value of the synchronism factor for some values of the cell numbers n : \bar{A} represents the mean of $|A|$ for hundred realizations of the stochastic process.

Table 4.8: \bar{A} for different values of the cells number n .

n	15	30	45	60	75	90
\bar{A}	0.997	0.989	0.975	0.958	0.935	0.906

We can see that the non-synchronism effect increases with the deflector length: in particular it can be of the order of 90% for very long deflectors, such as the high energy deflectors. For this reason, the total number of cells for the $(2/3)\pi$ deflector has been increased to 70, in order to obtain a deflecting voltage of 22.2 MV. In fact, in this way, even assuming a deflecting voltage degradation of 10%, $V_t=20$ MV is anyway achievable.

It is important to remark that the theoretical results shown in this section are valid for every statistical distribution of $\Delta\phi_e$.

4.6 Coupler design

In the travelling wave structures, a proper coupler design is required to excite the periodic field inside the cavity correctly, with the aim of minimizing the reflection coefficient. This can be done by varying the coupler dimensions w_c and r_c shown in Fig. 4.11, according to the shortcuts method reported in [30] and [31].

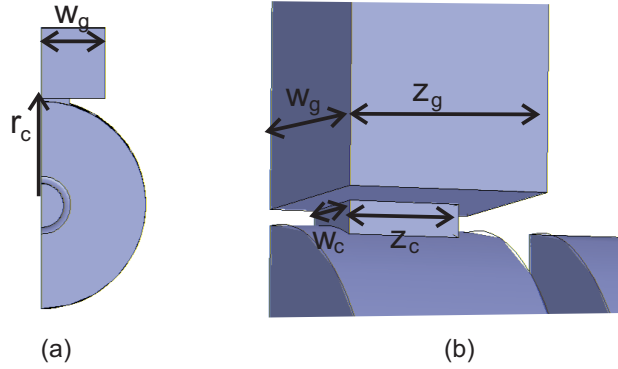


Figure 4.11: *Detail of the coupler of the travelling wave deflector.*

In fact, it can be shown that a necessary and sufficient condition to obtain critical coupling and the correct phase advance ϕ between the cells is given by:

$$\begin{cases} \alpha = \angle \frac{\Gamma_1}{\Gamma_0} = -2\varphi \\ \beta = \angle \frac{\Gamma_2}{\Gamma_1} = -2\varphi \end{cases} \quad (4.32)$$

where the symbol $\angle \Gamma_i$ for $i = 2, 1, 0$ denote the phase of the reflection coefficients evaluated with the model shown in Figs. 4.12 (a), (b) and (c), respectively. In particular, Fig. 4.12 (a) represents the coupler and a shortcut, Fig. 4.12 (b) represents the coupler, a cell and a shortcut and Fig. 4.12 (c) represents the coupler, two cell cell and a shortcut; let us note that the shortcut is composed by half of the basic cell closed by a perfect electric surface. Once the condition in equation (4.32) is met, where $\phi = (2/3)\pi$ in our case, the coupler satisfies the critical coupling and excites the correct

phase advance independently of the number n of cells of the periodic structure. Using the method described in [30] and [31], we obtained the critical coupling with $r_c=58.36$ mm and $w_c=17.14$ mm.

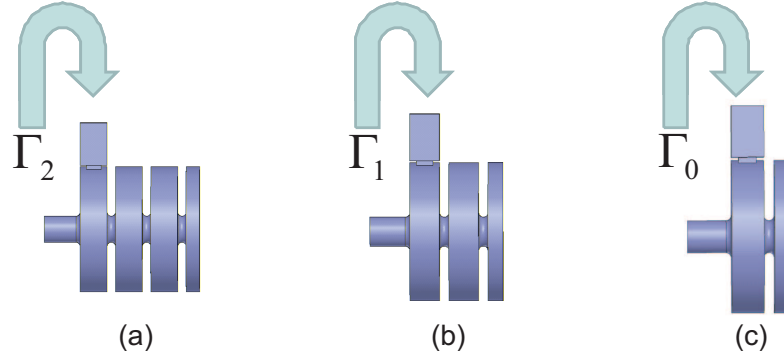


Figure 4.12: *Shortcut model used to excite the $(2/3)\pi$ mode in the travelling wave deflector.*

After finding these values of r_c and w_c , the coupler has been tested with the seven cells structure shown in Fig. 4.13, where the magnitude of the electric and magnetic field is put into evidence.

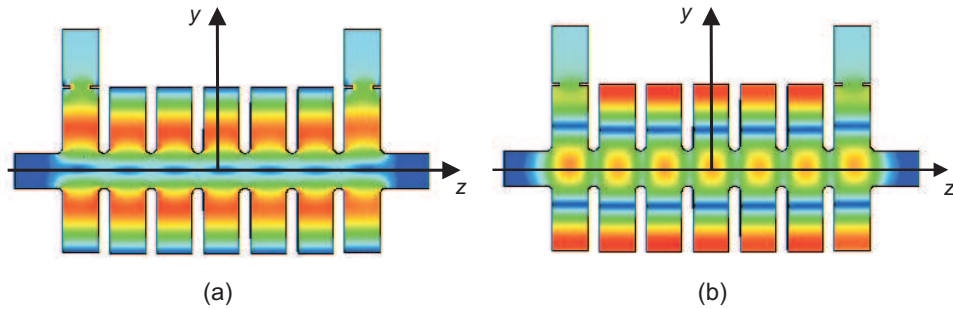


Figure 4.13: *The seven cell structure. (a) Electric field magnitude; (b) Magnetic field magnitude.*

Fig. 4.14 shows the scattering parameters s_{11} and s_{12} as a function of the frequency. At 2.998 GHz we have found $s_{11}=0.034$ and $s_{12}=0.96$.

As we have done in section 2.2, we show in Fig. 4.15 the absolute value of $E_{y,n} = \frac{|qE_y|}{\max(qcBx/\mu)}$ and $H_{x,n} = \frac{qcBx/\mu}{\max(qcBx/\mu)}$.

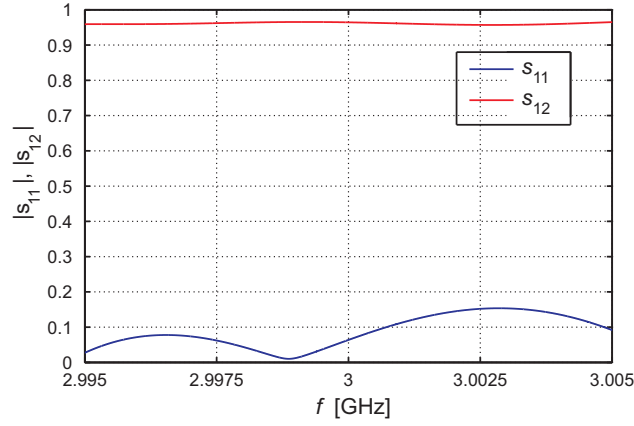


Figure 4.14: $|s_{11}|$ and $|s_{12}|$ as a function of the frequency f .

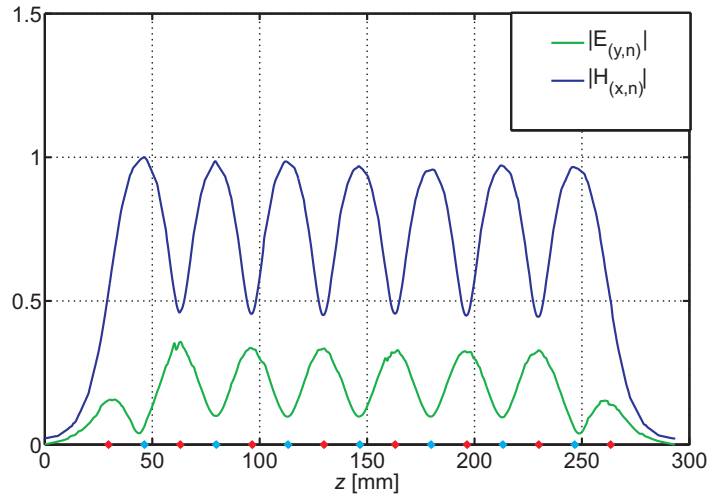


Figure 4.15: $|E_{y,n}|$ and $|H_{x,n}|$ evaluated on z axis as functions of the longitudinal deflector coordinate; the red and the blue points on the z axis represent the middle of the iris and the middle of the cells, respectively.

From Fig. 4.15 we can see that the magnetic field gives the most relevant contribution in the deflection. This is in agreement with the fact that, with an iris of $a=12.5$ mm, the group velocity is negative (Fig. 4.2), which means that the coupling between the deflector cells is essentially magnetic [9]. Furthermore, Fig. 4.15 shows that the electric field has a peak in the middle of

the iris, while the magnetic field has a peak in the middle of the cell.

Fig. 4.16 shows the phase of E_x and H_y along the seven cells deflector. We can see that the phase advance is periodic with $\phi=120$ deg. Furthermore, we can observe that the phases of E_x and H_x are flat in the middle of the iris and in the middle of the cell, respectively.

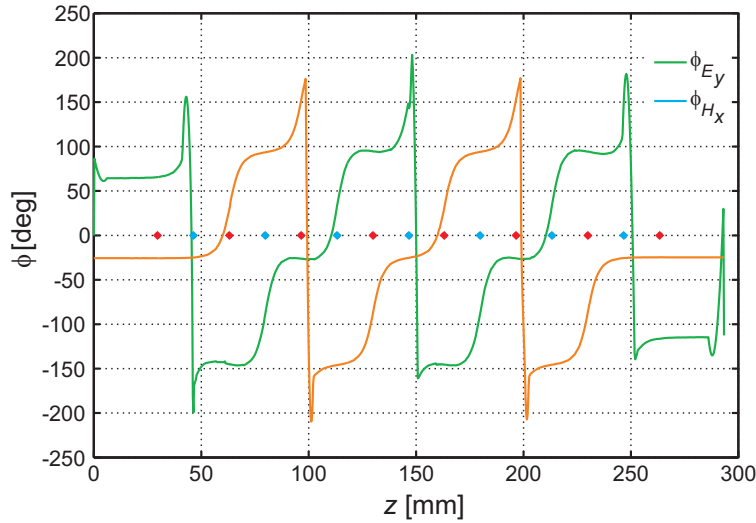


Figure 4.16: ϕ_{EY} and ϕ_{HX} as functions of the longitudinal deflector coordinate z ; the red and the blue points represent the middle of the iris and the middle of the cells, respectively.

The travelling wave deflector basic cells and the coupler are now under realization at PMB industry in Marseille (France) [32]. Fig. 4.17 shows the basic cell of the deflector, which has been realized in copper.

In order to validate the simulations, seven copper basic cells have been assembled and the resonant frequencies have been measured with a network analyzer. We can see in Fig. 4.18 that, as it was expected, the resonant frequencies are in excellent agreement with the dispersion diagram calculated with HFSS.

We show in Fig. 4.19 the deflector composed by seventy-two cells plus two couplers, which excite vertically the deflecting field. The deflector coupler is now being fine-tuned in order to excite properly the deflecting mode. After this procedure the cavity will be brazed and tested, and finally will operate at FERMI@Elettra to perform the beam diagnostic.

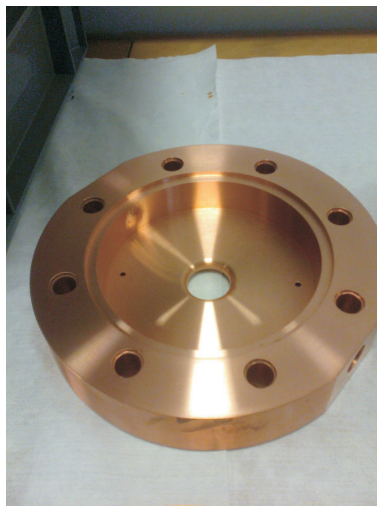


Figure 4.17: *Basic cell of the high energy deflector.*

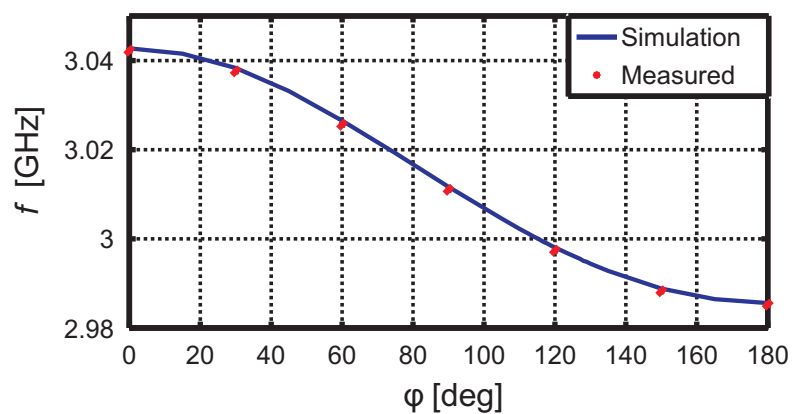


Figure 4.18: *Dispersion diagram obtained with HFSS and resonant frequencies assembling seven basic cells.*

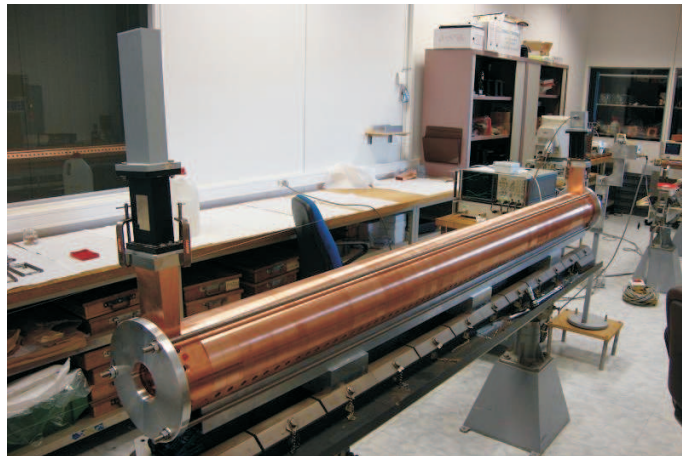


Figure 4.19: *High energy deflector composed by 72 cells plus two couplers.*

Chapter 5

Transversal Wakefield

5.1 Wakefield effect

If a point charge (called leading charge) travels at the speed of the light in a travelling wave disk loaded structure, and another charge or an electron bunch follows the leading charge, the electromagnetic field produced by the leading charge interacts with the metallic surfaces, and the scattering radiation, which is called wakefield, can reach the tail of the bunch, as shown in Fig. 5.1 [33]. In particular, if the bunch has an initial offset x_0 with respect to the z -axis, then the motion of the tail of the bunch is perturbed.

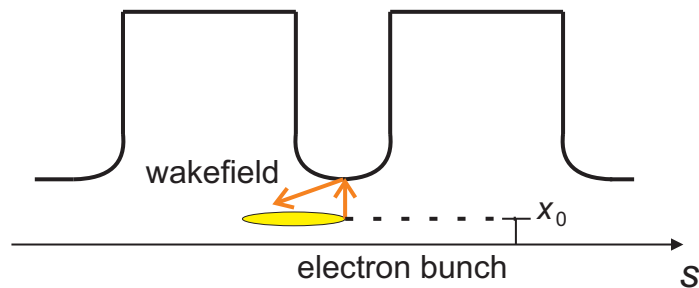


Figure 5.1: *The electromagnetic field produced by the head of the bunch scatters the metallic surfaces perturbing the tail of the bunch.*

Since the radio-frequency deflectors are used to measure parameters related to the electron bunch, we are interested in evaluating the perturbation produced by the wakefield effect during the bunch measurements. In particu-

lar, the two high energy deflectors described in chapter 4 have been designed with a small iris radius a in order to increase the deflecting voltage, as is shown in Fig. 4.5. Since the wakefield effect becomes more relevant when reducing the iris radius, this must be taken into account.

In our analysis the wakefield effect is considered introducing the transversal wake function W [34], which can be defined as the transverse field experienced by the test particle, divided by the unit charge e and by the transversal offset x_0 :

$$W(z) = \frac{\left[\vec{E}_s(z) + \vec{v} \times \vec{B}_s(z) \right]_t}{e x_0} \quad (5.1)$$

where (\vec{E}_s, \vec{B}_s) is the scattered electromagnetic field which perturb the bunch motion and \vec{v} is the particle speed.

The transversal wakefield effect has already been treated in the case of linear accelerators, where the travelling wave disk loaded structures are used to produce the TM_{010} accelerating mode and quadrupoles are used to stabilize a bunch in the design orbit [35]. In this case the transversal wakefield effect produces an instability which can lead the bunch out of the design orbit causing also an emittance growth. In particular, in [22] a perturbation method is applied to find a closed form solution for the simple case where a linear approximation of the wake function is used, together with a constant charge distribution of the bunch, a constant offset position and a constant angular divergence of the bunch at the input section of the accelerator. A different methodology has been recently used in [36], where an analytical approach is proposed to find closed form solutions to problems arising in the accelerators.

In this chapter we propose a new and accurate approach for the calculation of the transversal beam motion in a deflector [37]. This motion is described by an integro-differential equation which is different from that arising in the case of a linear accelerator, discussed in [22] and [36], where the forcing term is not present. The proposed algorithm discretizes the equation of the bunch motion, and then solves the discretized equation exactly. The algorithm can be applied to the general case of arbitrary charge distribution

and arbitrary boundary conditions of the bunch at the input section of the deflector.

5.2 Transversal beam dynamics

As a consequence of equation (1.49), the deflecting mode HEM_{11} produces, inside the iris, a transversal force given by

$$F_x(z) = \frac{eV_t}{l_{tot}} \sin(kz) \quad (5.2)$$

where k is the free space wave number, V_t is the deflecting voltage and e the electron charge. The local abscissa z represents the longitudinal position of an electron with respect to the center of the bunch. The beam is also subject to an additional transversal force, which is due to the wakefield effect and is given by

$$F_w(s, z) = e \int_z^{L/2} W(z' - z) \rho(z') x(s, z') dz' \quad (5.3)$$

where W is the wake function, and ρ the charge density of the bunch, so that the total bunch charge can be expressed as $Q = \int_{-L/2}^{L/2} \rho dz$. The (unknown) function $x(s, z)$ in (5.3) represents the transversal position of an electron located at the longitudinal position z inside the bunch, where the bunch center has distance s from the input section of the deflector. As a consequence, the transversal beam dynamics in presence of wakefield is described by the equation

$$\frac{\partial^2 x(s, z)}{\partial s^2} - \frac{e}{E_{tot}} \int_z^{L/2} W(z' - z) \rho(z') x(s, z') dz' = \frac{F_x(z)}{E_{tot}} \quad (5.4)$$

where E_{tot} is the energy of the electron. In absence of the wakefield effect, $F_w(s, z) = 0$. Thus, the solution of equation (5.4) is given by:

$$x(s, z) = \frac{eV_t}{l_{tot} E_{tot}} \frac{\sin(kz)}{2} s^2 + x'_0(z) s + x_0(z) \quad (5.5)$$

where:

$$x'_0(z) = \left. \frac{\partial x(s, z)}{\partial s} \right|_{s=0} \quad (5.6)$$

$$x_0(z) = x(s=0, z) \quad (5.7)$$

The terms $x_0(z)$ in (5.7) and $x'_0(z)$ in (5.6) represent the transversal position and the angular divergence, respectively, of the electron of local abscissa z , when the bunch center is located at the input section of the deflector ($s=0$).

We now propose a new simple algorithm that allows to solve equation (5.4) with arbitrary degree of accuracy, for any charge distribution $\rho(z)$ and for any boundary condition. We first approximate the equation by transforming the integral into a finite summation. Then the approximate equation is solved exactly, in a finite number of steps.

5.3 Determining the bunch motion

Since the variable z in (5.4) belongs to the interval $I_0 = [-L/2, L/2]$, it is convenient to divide I_0 into N adjacent subintervals of equal length $\Delta = L/N$, $I_i = [z_i, z_i + \Delta]$, where $z_i = -L/2 + (i-1)\Delta$ and $i = 1, \dots, N$. If N is sufficiently high (i.e., Δ is small), we can approximate the integral in (5.4) by a summation of N terms, thus the equation reduces to the following set of N differential equations:

$$\frac{\partial^2 x(s, z_i)}{\partial s^2} = \sum_{j=i+1}^N C_{j-i,j} x(s, z_j) + \frac{F_x(z_i)}{E_{tot}} \quad (5.8)$$

$i = 1, 2, \dots, N$, where

$$C_{p,n} = \frac{e\Delta}{E_{tot}} W(p\Delta) \rho(z_n) \quad (5.9)$$

It is to be noted that, as $W(0) = 0$ (see equation (5.24)), the coefficients $C_{0,n}$ in (5.9) are zero, thus the summation index j in (5.8) starts from $j = i+1$. Setting $i = N$, (5.8) becomes

$$\frac{\partial^2 x(s, z_N)}{\partial s^2} = \frac{F_x(z_N)}{E_{tot}} \quad (5.10)$$

whose solution is given by

$$x(s, z_N) = x_0(z_N) + x'_0(z_N) s + \frac{F_x(z_N)}{2E_{tot}} s^2 \quad (5.11)$$

Setting $i = N - 1$, equation (5.8) becomes

$$\frac{\partial^2 x(s, z_{N-1})}{\partial s^2} = C_{1,N} x(s, z_N) + \frac{F_x(z_{N-1})}{E_{tot}} \quad (5.12)$$

where $x(s, z_N)$ is given by (5.11). Substituting (5.11) into (5.12) and manipulating, yields:

$$x(s, z_{N-1}) = x_0(z_{N-1}) + x'_0(z_{N-1}) s + \frac{1}{2} C_{1,N} x_0(z_N) s^2 + \frac{1}{2} \frac{F_x(z_{N-1})}{E_{tot}} s^2 + \frac{1}{3!} C_{1,N} x'_0(z_N) s^3 + \frac{1}{4!} \frac{F_x(z_N)}{E_{tot}} s^4 \quad (5.13)$$

Reducing the index i progressively and proceeding in a similar way, the solution of the generic equation in (5.8), $x(s, z_i)$, is a polynomial of degree $2(N - i + 1)$, that is:

$$x(s, z_i) = \sum_{h=0}^{2(N-i+1)} X_{i,h} s^h \quad (5.14)$$

where the coefficients $X_{i,h}$ are to be determined. Such coefficients can be expressed in terms of the coefficients $X_{j,h}$ of higher order ($j = i + 1, i + 2, \dots, N$), corresponding to the solutions $x(s, z_{i+1}), \dots, x(s, z_N)$.

Suppose that such coefficients $X_{j,h}$ are known. Substituting (5.14) (with i replaced by j) into (5.8) and manipulating, yields the equation:

$$\frac{\partial^2 x(s, z_i)}{\partial s^2} = \sum_{k=0}^{2N-2i} \left(\sum_{j=i+1}^{M[k,N]} C_{j-i,j} X_{j,k} \right) s^k + \frac{F_x(z_i)}{E_{tot}} \quad (5.15)$$

where

$$M[k, N] = \text{Int} [\text{Min} \{N, N + 1 - k/2\}] \quad (5.16)$$

In (5.16), $\text{Int} [\]$ denotes the integer part. For any $i = N-1, N-2, \dots, 2, 1$, the solution of (5.15) is given by (5.14), where it can be verified that the coefficients are given by:

$$X_{i,0} = x_0(z_i) \quad (5.17)$$

$$X_{i,1} = x'_0(z_i) \quad (5.18)$$

$$X_{i,2} = \frac{1}{2} \left(\sum_{j=i+1}^N C_{j-i,j} X_{j,0} + \frac{F_x(z_i)}{E_{tot}} \right) \quad (5.19)$$

$$X_{i,h} = \frac{1}{h(h-1)} \sum_{j=i+1}^{M[h-2,N]} C_{j-i,j} X_{j,h-2} \quad (5.20)$$

for $3 \leq h \leq 2(N-i+1)$. Using (5.14), we can calculate the angular divergence, defined as the derivative

$$\frac{\partial x(s, z_i)}{\partial s} = \sum_{h=1}^{2(N-i+1)} h X_{i,h} s^{h-1} \quad (5.21)$$

5.4 Numerical examples

In this section we will apply the method described in section 5.3 to the high energy deflectors working in the $(2/3)\pi$ mode, which have the geometrical basic cell parameters reported in Table 4.2. In the following examples we will assume that the deflectors will operate at high energy ($E_{tot} = 1.2$ GeV), with an electron bunch of total charge $Q = 1$ nC and length $L = 450$ μm .

The ideal motion of an electron bunch (equation (5.5)) in the case $V_t = 20$ MV, $L = 450$ μm , and $x_0(z) = x'_0(z) = 0$, is shown in Fig. 5.2. The upper black line corresponds to the head (H) of the bunch, while the lower black line to the bunch tail (T). The lines in between represent the middle part of the bunch and in particular the cyan line is the center (C). The same color notation has been used in Figs. 5.2, 5.3, 5.4, 5.5, 5.7, 5.8, 5.9 and 5.10. We have performed our simulation setting $N = 70$ in equation (5.8), which allows a good accuracy as it will be shown in section 5.5. Fig. 5.3 shows the ideal straight lines of the bunch divergence, again in the case $V_t = 20$ MV, $L = 450$ μm and $x_0(z) = x'_0(z) = 0$.

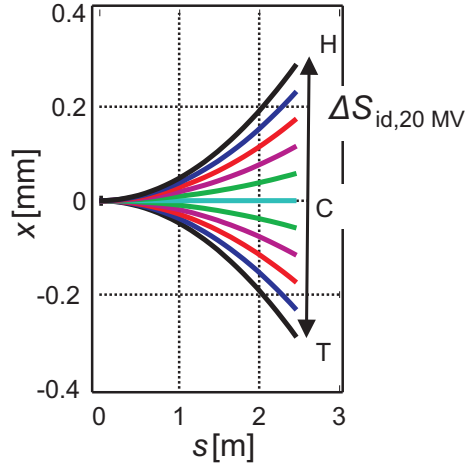


Figure 5.2: *Ideal transversal bunch motion for $L = 450$ μm , $V_t = 20$ MV and $x_0(z) = x'_0(z) = 0$.*

In the FERMI@Elettra layout the two deflectors are separated by a drift of 1.4 meters. For this reason we will analyze also the case where the first deflector is "on", and the second one is "off". The ideal motion is shown in Fig. 5.4, while the ideal angular divergence is shown in Fig. 5.5 ($L = 450$

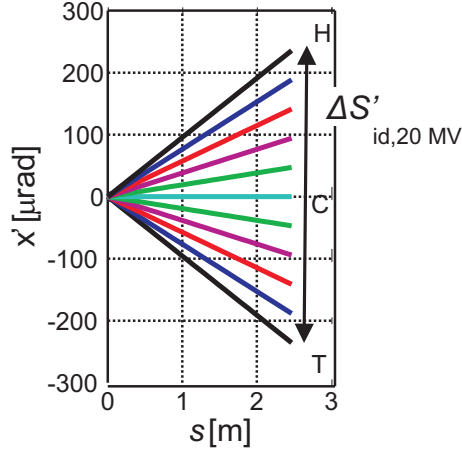


Figure 5.3: *Ideal angular divergence for $L = 450 \mu\text{m}$, $V_t=20 \text{ MV}$ and $x_0(z) = x'_0(z) = 0$.*

μm , $V_t = 20 \text{ MV}$ and $x_0(z) = x'_0(z) = 0$). The two deflectors and the drift are indicated with the symbols D1, D2 and Dr, respectively. The drift is located between the two marked vertical lines in Figs. 5.4 and 5.5; the same notation has been used in Figs. 5.9 and 5.10. Fig. 5.4 shows that the ideal parabolic motion in D1 becomes a straight line in Dr and D2. The ideal angular divergence in Fig. 5.5 is a straight line in D1, and remains constant in Dr and D2.

We have reported in Table 5.1 the ideal spread between the head and the tail of the bunch (head-tail effect), defined as

$$\Delta S_{\text{id}, \bar{V}_t} = x(l_{\text{tot}}, L/2) - x(l_{\text{tot}}, -L/2) \quad (5.22)$$

and the ideal angular spread between the head and the tail of the bunch, defined as

$$\Delta S'_{\text{id}, \bar{V}_t} = x'(l_{\text{tot}}, L/2) - x'(l_{\text{tot}}, -L/2) \quad (5.23)$$

These parameters have been calculated considering two bunches having $L = 150 \mu\text{m}$ and $L = 450 \mu\text{m}$, with the deflecting voltage taking the values $\bar{V}_t = 5, 10$ and 20 MV . In Table 5.1, columns D1, the spreads are those

evaluated at the output section of the first deflector, while the spreads in the columns D2 are those evaluated at the output section of the second deflector. Table 5.1 shows that the angular divergence does not increase during the motion in the second deflector.

We are now interested in evaluating the variation of the parameters

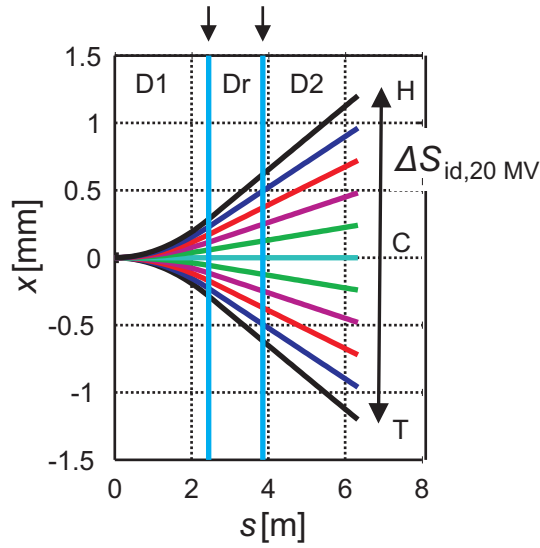


Figure 5.4: Ideal transversal bunch motion in the case $L = 450 \mu\text{m}$, $V_t = 20 \text{ MV}$ in the deflector $D1$ and $V_t = 0$ in the deflector $D2$.

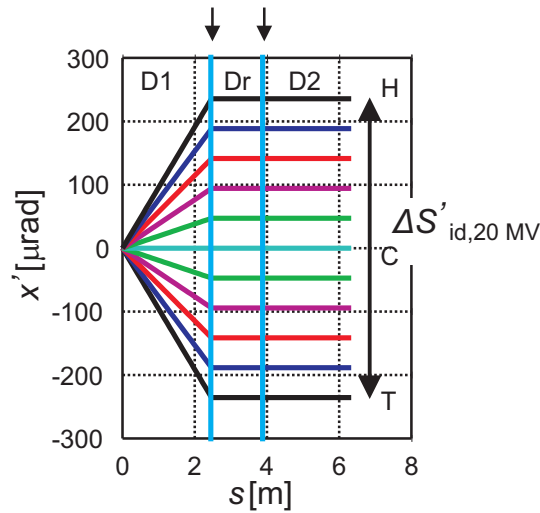


Figure 5.5: Ideal angular divergence in the case $L = 450 \mu\text{m}$, $V_t = 20 \text{ MV}$ in the deflector $D1$ and $V_t = 0$ in the deflector $D2$.

	$L= 150\mu\text{m}$		$L= 450\mu\text{m}$	
	D1	D2	D1	D2
$\Delta S_{id,5MV} [\mu\text{m}]$	48	200	145	601
$\Delta S_{id,10MV} [\mu\text{m}]$	97	400	291	1202
$\Delta S_{id,20MV} [\mu\text{m}]$	194	801	581	2403
$\Delta S'_{id,5MV} [\mu\text{rad}]$	39	39	118	118
$\Delta S'_{id,10MV} [\mu\text{rad}]$	78	78	236	236
$\Delta S'_{id,20MV} [\mu\text{rad}]$	157	157	471	471

Table 5.1: *Ideal head-tail effects and angular spreads.*

$\Delta S_{id,\bar{v}_t}$ and $\Delta S'_{id,\bar{v}_t}$ produced by the wakefield effect. In particular, the angular spread results to be proportional to the vertical trace ΔX_s according to equation (1.53), as represented in Fig. 1.7. Thus, an error on the angular spread, due to the wakefield, affects the accuracy of a bunch length measurement.

In the calculations we used the expression proposed in [34] for the wake function, which holds true for short bunches, given by

$$W(z) = \frac{4Z_0cs_{00}}{\pi a^4} \left[1 - \left(1 + \sqrt{\frac{z}{s_{00}}} \right) e^{-\sqrt{\frac{z}{s_{00}}}} \right] \quad (5.24)$$

where $Z_0 = 120\pi \Omega$ is the intrinsic impedance of the free space,

$$s_{00} = \frac{g}{8} \left(\frac{a}{L\alpha(g/L)} \right)^2 \quad (5.25)$$

with $\alpha(\zeta)$ a dimensionless function defined as

$$\alpha(\zeta) = 1 - \alpha_1 \sqrt{\zeta} - (1 - 2\alpha_1) \zeta \quad (5.26)$$

where $\alpha_1 = 0.4648$. Furthermore, we have considered the two charge distributions B_1 and B_2 shown in Fig. 5.6. B_1 is a constant distribution, while B_2 has an head-accumulated shape. The plots in Fig. 5.6 have been traced using a normalized distance $z_N = z/L$ and a normalized charge density $\rho_N = L\rho/Q$.

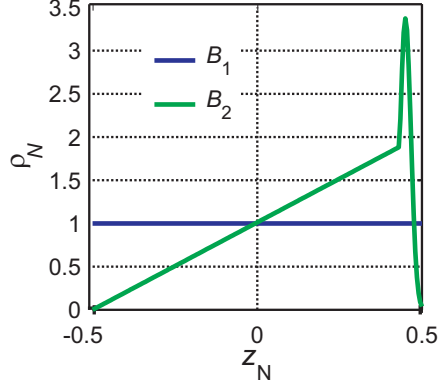


Figure 5.6: Normalized charge density profiles B_1 and B_2 .

We now define the two quantities

$$e_{S,\bar{v}_t} = \frac{\Delta S_{\text{id},\bar{v}_t} - \Delta S_{\bar{v}_t}}{\Delta S_{\text{id},\bar{v}_t}} \quad (5.27)$$

and

$$e_{D,\bar{v}_t} = \frac{\Delta S'_{\text{id},\bar{v}_t} - \Delta S'_{\bar{v}_t}}{\Delta S'_{\text{id},\bar{v}_t}} \quad (5.28)$$

Such quantities are, respectively, the relative error due to the wakefield effect on the head-tail spread and the relative error on the angular spread, where $\Delta S_{\bar{v}_t}$ and $\Delta S'_{\bar{v}_t}$ are the real spreads, affected by the wakefield. We have reported in Tables 5.2 and 5.3 the relative errors e_{S,\bar{v}_t} and e_{D,\bar{v}_t} , calculated after the first deflector for a bunch having $L = 150 \mu\text{m}$ and $L = 450 \mu\text{m}$, respectively, with charge distributions B_1 and B_2 . The initial conditions of the bunch are $x_0 = 1.5, 3 \text{ mm}$ and $x'_0 = 0$.

The bunch motion and the angular divergence in the worst case, corresponding to $L = 150 \mu\text{m}$, $V_t=5 \text{ MV}$, charge distribution B_2 and $x_0 = 3 \text{ mm}$, have been plotted in Figs. 5.7 and 5.8. We can see that $x(s, z)$ and $x'(s, z)$ have lost their symmetry with respect to the center of the bunch. In particular, in both cases the lower black line (corresponding to the tail of the bunch) raises its position, thus the head-tail effect and the angular spread decrease compared to the ideal case.

		$x_0 = 1.5\text{mm}$		$x_0 = 3\text{mm}$	
		B_1	B_2	B_1	B_2
$e_{S,5MV}$	[%]	2.3	3.1	4.7	6.2
$e_{S,10MV}$	[%]	1.2	1.6	2.5	3.2
$e_{S,20MV}$	[%]	0.57	0.77	1.2	1.5
$e_{D,5MV}$	[%]	2.5	3.3	4.8	6.4
$e_{D,10MV}$	[%]	1.1	1.5	2.3	3.1
$e_{D,20MV}$	[%]	0.63	0.83	1.2	1.6

Table 5.2: Relative errors on the head-tail effect and on the angular spread, calculated after the first deflector in the case $L = 150 \mu\text{m}$.

		$x_0 = 1.5\text{mm}$		$x_0 = 3\text{mm}$	
		B_1	B_2	B_1	B_2
$e_{S,5MV}$	[%]	2.1	2.7	4.1	5.3
$e_{S,10MV}$	[%]	1.0	1.3	2.1	2.7
$e_{S,20MV}$	[%]	0.52	0.69	1.0	1.3
$e_{D,5MV}$	[%]	2.0	2.6	4.1	5.3
$e_{D,10MV}$	[%]	1.0	1.4	2.1	2.7
$e_{D,20MV}$	[%]	0.51	0.68	1.0	1.3

Table 5.3: Relative errors on the head-tail effect and on the angular spread, calculated after the first deflector in the case $L = 450 \mu\text{m}$.

Now we consider the case where the bunch, stretched by the first deflector, passes through the drift and the second deflector. Tables 5.4 and 5.5 show the relative errors e_{S,\bar{v}_t} and e_{D,\bar{v}_t} calculated after the second deflector, for $L = 150 \mu\text{m}$ and $L = 450 \mu\text{m}$, respectively.

The transversal bunch motion and the angular divergence in the worst case, corresponding to $L = 150 \mu\text{m}$, $V_t = 5 \text{ MV}$, charge distribution B_2 and $x_0 = 3 \text{ mm}$, have been plotted in Figs. 5.9 and 5.10, respectively. We can see the lack of the symmetry with respect to the bunch center, due to the wakefield in both the deflectors.

Tables 5.2, 5.3, 5.4 and 5.5, suggest the following considerations on the transversal wakefield in a microwave deflector. The wakefield effects are inversely proportional to the deflecting voltage applied to the electron bunch.

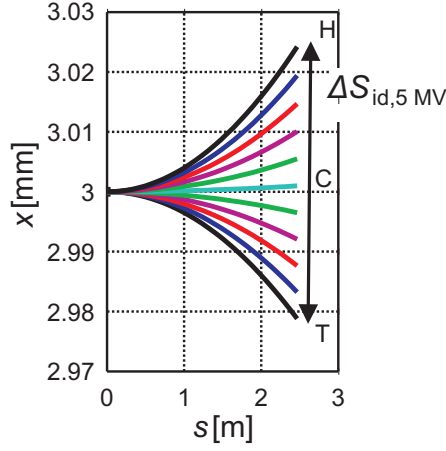


Figure 5.7: *Transversal bunch motion in the case $L = 150 \mu\text{m}$, charge density B_2 , $x_0 = 3 \text{ mm}$ and $V_t = 5 \text{ MV}$.*

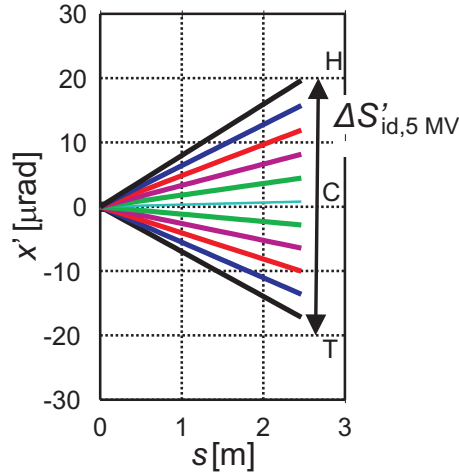


Figure 5.8: *Angular divergence in the case $L = 150 \mu\text{m}$, charge density B_2 , $x_0 = 3 \text{ mm}$ and $V_t = 5 \text{ MV}$.*

This can be explained observing that, in the solution (5.14), the coefficients $X_{i,0}$ and $X_{i,2}$ are dominant over the others, that is, the motion of the particles is approximately parabolic. Furthermore, the coefficient $X_{i,2}$ in (5.19) consists of two terms. The first one is $\frac{1}{2} \sum_{j=1+1}^N C_{j-i,j} X_{j,0}$, and represents the perturbation given by the initial offset $x_0(z)$. This term depends on the charge density and on the wake function. The second term is $\frac{1}{2} \frac{F_x(zi)}{K_{tot}}$, which represents the ideal motion in absence of wakefield, and depends only on the

		$x_0 = 1.5\text{mm}$		$x_0 = 3\text{mm}$	
		B_1	B_2	B_1	B_2
$e_{S,5MV}$	[%]	3.0	3.9	6.0	7.8
$e_{S,10MV}$	[%]	1.5	1.9	3.0	3.9
$e_{S,20MV}$	[%]	0.75	0.99	1.5	2.0
$e_{D,5MV}$	[%]	4.8	6.4	9.7	12.7
$e_{D,10MV}$	[%]	2.4	3.2	4.8	6.2
$e_{D,20MV}$	[%]	1.3	1.6	2.5	3.2

Table 5.4: *Relative errors on the head-tail effect and on the angular spread, calculated in the case where $L = 150 \mu\text{m}$ and the two deflectors are separated by a drift.*

		$x_0 = 1.5\text{mm}$		$x_0 = 3\text{mm}$	
		B_1	B_2	B_1	B_2
$e_{S,5MV}$	[%]	2.6	3.3	5.1	6.6
$e_{S,10MV}$	[%]	1.3	1.7	2.6	3.4
$e_{S,20MV}$	[%]	0.67	0.87	1.3	1.7
$e_{D,5MV}$	[%]	4.2	5.5	8.3	10.8
$e_{D,10MV}$	[%]	2.2	2.8	4.2	5.5
$e_{D,20MV}$	[%]	1.1	1.5	2.2	2.8

Table 5.5: *Relative errors on the head-tail effect and on the angular spread, calculated in the case where $L = 450 \mu\text{m}$ and the two deflectors are separated by a drift.*

applied deflecting voltage. Thus, when the deflecting voltage increases, the second term increases and dominates over the first one, which remains constant. As a consequence, the wakefield effect decreases and also the relative error decreases.

From Tables 5.2, 5.3, 5.4 and 5.5, we can observe that the wakefields are more relevant in the case $L = 150 \mu\text{m}$ (small bunch). In fact, the deflecting voltage V_t is proportional to $\sin(kz)$ by (5.2), where $|z| \leq L/2$ and $|kL/2| \ll 1$. Thus, increasing the bunch length produces a greater deflecting force, and the wakefield effect is mitigated.

Furthermore, we can observe that $e_{S,\bar{v}_t} \cong e_{D,\bar{v}_t}$ in the case where only

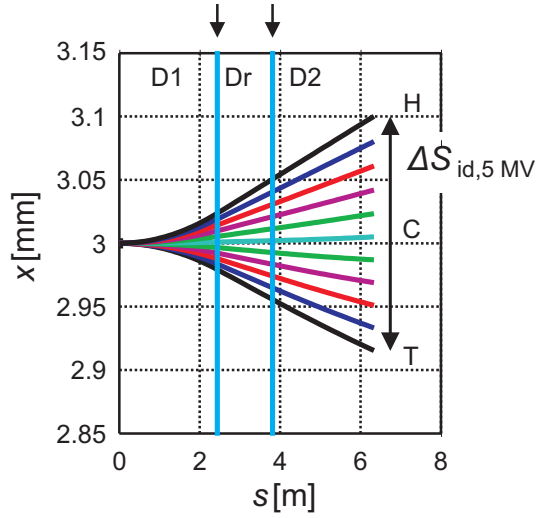


Figure 5.9: *Transversal bunch motion in the case $L = 150 \mu\text{m}$, charge density B_2 , $x_0 = 3 \text{ mm}$, $V_t = 5 \text{ MV}$ in the deflector $D1$ and $V_t = 0$ in the deflector $D2$.*

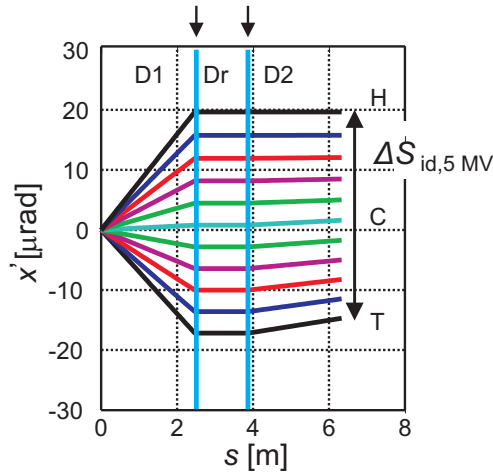


Figure 5.10: *Angular divergence in the case $L = 150 \mu\text{m}$, charge density B_2 , $x_0 = 3 \text{ mm}$, $V_t = 5 \text{ MV}$ in the deflector $D1$ and $V_t = 0$ in the deflector $D2$.*

one deflector is considered. Instead, in the case where two deflectors are considered, we have $e_{D,\bar{v}_t} > e_{S,\bar{v}_t}$. This is important since, as it was previously noted, e_{D,\bar{v}_t} is proportional to the relative error on a bunch length measurement. As a last consideration, we can note that, in the case where only one deflector is considered, a deflecting voltage $V_t = 5 \text{ MV}$ is sufficient to protect the bunch motion from the wakefield effect. Instead, in the case where two

deflectors are considered, a deflecting voltage $V_t = 10$ MV is advisable if a considerable initial offset x_0 is present.

5.5 Evaluating the convergence

In order to numerically evaluate the convergence of the presented method, we first determine an approximation $x_a(s, z)$ of the solution $x(s, z)$ of equation (5.4), by linearly interpolating the samples $x(s, z_i)$, where $z_i = -L/2 + (i-1)\Delta$, with $\Delta = L/N$. This allows to estimate the first term of the left-hand side in (5.4) as

$$I = \frac{\partial^2 x_a(s, z)}{\partial s^2} \quad (5.29)$$

Then we calculate the integral in (5.4). To this aim, we divide each interval $I_i = [z_i, z_i + \Delta]$ into M adjacent subintervals of length $\Delta' = \Delta/M = L/MN$. Thus we obtain MN intervals $I'_i = [z'_i, z'_i + \Delta']$, $z'_i = -L/2 + (i-1)\Delta'$, $i = 1, \dots, MN$. The middle point of $I'_i = [z'_i, z'_i + \Delta']$ is $z_i^m = z'_i + \Delta'/2$. The second term in the left hand-side of (5.4) is then approximated by

$$II = \frac{e}{E_{tot}} \Delta' \sum_{r=l}^{MN} W(z_r^m - z) \rho(z_r^m) x_a(s, z_r^m) \quad (5.30)$$

where l is such that $I'_l = [z'_l, z'_l + \Delta']$ is the interval containing the point z . The right-hand side of equation (5.4) is given by

$$III = \frac{F_x(z)}{E_{tot}} \quad (5.31)$$

Thus we can introduce the relative convergence error

$$e_{conv} = \frac{I - II - III}{I - II} \quad (5.32)$$

We now evaluate the convergence of our algorithm with reference to the cases $L = 150 \mu\text{m}$ and $L=450 \mu\text{m}$, an initial offset of $x_0=3$ mm and the

density charge distribution B_1 , using the deflecting voltages $V_t=10$ and $V_t=20$ MV. Subsequently, we evaluate the relative convergence error at the end of the bunch. The discretization step N has been varied from 10 to 300, using $M = 30$ subintervals. The convergence error is shown in Tables 5.6 and 5.7.

N	$e_{conv, V_t=10MV}$	$e_{conv, V_t=20MV}$
10	$4.7 \cdot 10^{-3}$	$2.3 \cdot 10^{-3}$
50	$9.3 \cdot 10^{-4}$	$4.6 \cdot 10^{-4}$
100	$4.7 \cdot 10^{-4}$	$2.3 \cdot 10^{-4}$
200	$2.3 \cdot 10^{-4}$	$1.1 \cdot 10^{-4}$
300	$1.5 \cdot 10^{-4}$	$7.6 \cdot 10^{-5}$

Table 5.6: *Convergence evaluation for a bunch B_1 having $L = 150 \mu\text{m}$, $M = 30$, $x_0 = 3 \text{ mm}$.*

N	$e_{conv, V_t=10MV}$	$e_{conv, V_t=20MV}$
10	$3.8 \cdot 10^{-3}$	$1.8 \cdot 10^{-3}$
50	$7.4 \cdot 10^{-4}$	$3.5 \cdot 10^{-4}$
100	$3.7 \cdot 10^{-4}$	$1.7 \cdot 10^{-4}$
200	$1.8 \cdot 10^{-4}$	$8.7 \cdot 10^{-5}$
300	$1.2 \cdot 10^{-4}$	$5.8 \cdot 10^{-5}$

Table 5.7: *Convergence evaluation for a bunch B_1 having $L = 450 \mu\text{m}$, $M = 30$, $x_0 = 3 \text{ mm}$.*

We can observe from Tables 5.6, 5.7 that the convergence is good both for the short and the long bunch. In particular a discretization step $N=50$ is sufficient to obtain a convergence error $e_{conv} < 10^{-3}$ for both the deflecting voltages considered.

Conclusion

In this thesis the radio-frequency design of the low energy deflector and the high energy deflector are presented. The low energy radio-frequency deflector, which is a five cell standing wave cavity developed in collaboration with SPARC Laboratory of Frascati and the University La Sapienza (Rome), has been already realized and installed in the FERMI@Elettra project.

The cavity has performed the first operations with the electron bunches evaluating the bunch length in the last months of 2010. With the low energy deflector the different shape of the longitudinal profiles of the uncompressed and compressed bunch have been compared. In particular, it has been observed that the parabolic shape of the uncompressed bunch becomes triangular when the bunch compressor is operating, and the increase of the peak current has been evaluated. In this way, the longitudinal current profiles of both the uncompressed and the compressed bunches have been reconstructed, providing an efficient diagnostic for the beam which has been used in December 2010 to produce the first free electron laser at FERMI@Elettra. During the bunch measurements the optical transport coefficient R_{34} has been evaluated with an indirect measurement. Thus, the optical design of the bunch compressor area has been confirmed with good accuracy, for both the uncompressed and the compressed bunch.

Using the low energy deflector also the emittance slice evaluation of the uncompressed bunch has been possible. In particular, we have observed an increasing of emittance and of the betatron function from the head to the tail of the bunch, which could be induced by the transversal wakefield of the previous linac 1 section.

Regarding the high energy deflectors, the prototype is now under construction, and the first radio-frequency measurements on the basic cell have

confirmed the predicted values. When the cavities will be installed and will operate, the electron bunches will be measured in both planes just before the production of the free electron laser, in the most strategic position for a IV generation light source as FERMI@Elettra.

Furthermore, a theoretical insight in the energy exchange between the electromagnetic field and the electron bunch has been given. An useful statistical model to describe the effects of mechanical errors in the realization of the deflector basic cell has been proposed. With this method, which is valid for every statistical distribution of the errors, the decrease of the deflecting voltage can be easily estimated for the travelling wave deflectors having an arbitrary number of cells. In this way, a safety margin for the deflecting voltage can be taken into account during the radio-frequency design, as we have done for the high energy deflectors.

In the last part of the thesis, the instability effect produced by the wakefields on the electron bunch motion has been investigated with a new numerical algorithm. The differential equation of the transversal beam dynamics has been discretized, and with an iteration method the exact solution of the discretized differential equation has been obtained. With the algorithm we can easily take into account of any charge distribution, and of any initial condition of the bunch at the input section of the cavity. It has been observed with the numerical simulations that smaller bunches are more sensitive than longer bunches with respect to the transversal wakefield. Using the proposed method we can consider also the case in which the electron bunch travels in both the high energy deflectors, and the minimum amount of deflecting voltage required to guarantee the correct behavior of the high energy deflector as a beam diagnostic tool has been estimated. The analysis of the transversal wakefield in the radio-frequency deflectors is concluded with the evaluation of the convergence of the method.

Ringraziamenti

Desidero ringraziare l'Università degli Studi di Trieste e la Sincrotrone Trieste S.C.p.A. per avermi dato la possibilità di intraprendere questo Dottorato di Ricerca. In particolare un caloroso grazie va al Prof. Roberto Vescovo e al Dr. Paolo Craievich per il forte sostegno e impulso che mi hanno dato nel corso della mia attività di ricerca.

Tra le persone che mi hanno aiutato in questi tre anni, una menzione speciale spetta al Dr. Alberto Lutman, per il suo prezioso supporto nella creazione delle interfacce grafiche in Matlab e nelle tecniche di rimozione del rumore. Un grazie anche al Dr. Giuseppe Penco per il suo positivo e costante sprone durante i turni svolti nella control room.

Ricorderò inoltre con piacere le utili discussioni avute con Simone Spampinati, Simone Di Mitri, Mauro Trovò, Luca Giannessi, Roberto Appio, Marco Veronese, Davide Castronovo, Enrico Allaria, Massimo Dal Forno, Defa Wang, Daniele La Civita, Youssef Kharoubi.

Infine, desidero ringraziare Antonella, i miei genitori e la mia famiglia per il continuo affetto e incoraggiamento.

Bibliography

- [1] FERMI@ELETTRA, *Conceptual Design Report*, Sincrotrone Trieste, Trieste, Italy, 2007.
- [2] H.Hahn, *Deflecting mode in iris-loaded waveguides*, Rev. Sci. Instr. 34, 10, 1963.
- [3] W.K.H. Panofsky, W.A. Wenzell, *Some considerations concerning the transverse deflection of charged particles in radio frequency- fields*, Rev. Sci. Instr. 27, 967, 1956.
- [4] P.Emma, J.Frisch, P. Krejcik, *A transverse RF deflecting structure for bunch length and phase diagnostic* , Springer-Verlag, 2000.
- [5] G.A.Loew, O.H. Altenmuller, *Design and application of RF separator structures at SLAC*, Stanford linear accelerator center, Stanford University Stanford, California, 1965.
- [6] M.Puglisi, *Conventional RF Cavity Design*, Sincrotrone Trieste, Trieste, Italia, 1991.
- [7] R.E. Collin, *Foundations for Microwave Engineering, Second Edition*, Donald G. Dudley Series Editor, 1992.
- [8] M.J. Brownmann, *Using the Panofsky-Wenzel theorem in the analysis of the radio-frequency deflectors*, Los Alamos National laboratory, 1993.
- [9] T.P. Wangler, *Introduction to linear accelerator, Revision 2*, Los Alamos National Laboratory, 1994.

- [10] H. Wiedemann, *Particle Accelerator Physics, Basic Principles and Linear Beam Dynamics*, Springer-Verlag, 1993.
- [11] J. Rossbach and P. Schmuser, *Basic course on accelerator optics*, Cern Accelerator School, 1992.
- [12] P. Craievich, S. Biedron, C. Bontoiu, S. Di Mitri, M. Ferianis, M. Veronese, M. Petronio, D. Alesini, L. Palumbo, L. Ficcadenti, *Fermi Low-Energy Transverse RF Deflector*, Proc. of Epac 2008, Genoa, Italy, June 23-27 2008, pp. 1239-1241.
- [13] P. Craievich, S. Biedron, D. La Civita, M. Ferianis, M. Petronio, R. Vescovo, D. Alesini, L. Palumbo, L. Ficcadenti, *A Low-Energy RF Deflector for the FERMI@Elettra project*, Proceedings of FEL 2010, Malmo, Sweden, (2010).
- [14] www.ansoft.com
- [15] L.C. Maier Jr. and J.C. Slater, *Field strength measurement in resonant cavities*, Journal of Applied Physics, 23, 1 (1951).
- [16] D. Alesini et al., *Design and RF measurements of an X-band accelerating structure for linearizing the longitudinal emittance at SPARC*, Nuclear Instruments and Methods in Physics Research A 554, pp. 1-12, (2005).
- [17] S. Di Mitri, *Compact multi-purpose optics insertion in the FERMI@Elettra linac bunch compression area*, Proceedings of FEL 2010, Malmo, Sweden, (2010).
- [18] M. Borland, APS Light Source Note, LS-287, (2000).
- [19] P. Craievich, R. De Monte, T. Borden, A. Borga, M. Ferianis, M. Predonzani, M. Dal Forno, R. Vescovo, *Cavity BPM Design, Simulations and Testing for the FERMI@ELETTRA Project*, FEL 2010, Malmo, Sweden.
- [20] P. Craievich, S. Di Mitri, M. Ferianis, M. Veronese, M. Petronio, D. Alesini, *A Transverse RF Deflecting Cavity for the FERMI@ELETTRA Project*, DIPAC 2007, Trieste, Italy.

- [21] M. Minty, *Beam Diagnostic*, Synchrotron Radiation and Free Electron Laser Course, Cern Accelerator School, 2003.
- [22] A. W. Chao, B. Richter and C. Yao, *Beam Emittance Growth Caused by Transverse Deflecting Fields in a Linear Accelerator*, Nuclear Instruments and Methods, **178** (1980) 1.
- [23] Y.Garault, *Etude d'une classe d'ondes electromagnetiques guidees: les ondes EH, applications aux structures deflectrices pour les separateurs a onde progressive de particules relativistes*, CERN, Ginevra, 1964.
- [24] G.A.Loew, R.R. Larsen, O.H. Altenmuller, *Investigation of travelling wave separators for the Stanford two-mile linear accelerator*, International Conference on high Energy Accelerators at Dubna, U.S.S.R., 1963.
- [25] P.Bernard, H.Lengeler, V.Vaghin, *On the design of disc-loaded waveguides for rf separators*, CERN, Ginevra, Svizzera e Institute of high-energy physics, Sepurkhov, USSR, 1968.
- [26] J.A.Aleksandrov, V.Vaghin, V.Kotov, *On properties of hybrid waves in a disc-loaded waveguide*, CERN, Ginevra, 1966.
- [27] M. Petronio, *Progetto di una cavità deflettente per la diagnostica di un laser ad elettroni liberi*, Tesi di Laurea, Università degli Studi di Trieste, (2006).
- [28] P. Craievich, M. Petronio, R. Vescovo, *Deflecting Mode Optimization for a High Energy Beam Diagnostic Tool*, Proceedings of Pac 2009, Vancouver, Canada, (2009).
- [29] M. Petronio, R. Vescovo, P. Craievich, *Perturbazione del campo elettromagnetico in una struttura periodica impiegata per la deflessione di pacchetti di elettroni*, Atti della Rinem 2008, Lecce, Italia, (2008).
- [30] A. Marinelli, *Progetto di un accoppiatore in guida d'onda per una struttura accelerante ad onda viaggiante in banda X*, Tesi di Laurea, Università La Sapienza di Roma, (2004).

- [31] D. Alesini, A. Gallo, B. Spataro, A. Marinelli, L. Palumbo, *Design of input coupler for travelling wave structures*, Technical Note, SPARC-RF-07/2001, (2007).
- [32] <http://www.alcen.com/en/pmb.php>
- [33] P.B. Wilson, *Introduction to Wakefield and Wake-Potential*, SLAC-PUB 4547, (1989).
- [34] K. L.F. Bane and M. Sands, *Particle Accelerator*, Vol. 25, Gordon and Breach, Science Publisher, Inc., United States of America, (1990).
- [35] A. W. Chao, *Physics of Collective Beam Instabilities*, John Wiley and Sons, New York, (1993).
- [36] J.R. Delayen, *Cumulative Beam Breakup in Linear Accelerators with Arbitrary Beam Current Profile*, Physical Review Special Topic-Accelerators and Beams, **6** (2003) 1.
- [37] M. Petronio, R. Vescovo, P. Craievich, *Analysis of the instability effect produced by the transversal wakefields on a ultra-relativistic electron bunch travelling in a microwave deflector*, Atti della Rinem 2010, Benevento, Italia,(2010).